Development of Brain Activity Measurement System based on Highly Sensitive Magneto-Impedance Sensor

March 2018

WANG Kewang

Graduate School of Engineering
Nagoya University

Table of Contents

Chapter 1

Introduction

1.1 Background and Motivation

"What's the meaning of life?", "What makes us human?" Centuries passed but there have always been some core questions of human beings and those questions are realized because of the brain. Our brain is considered as the most complex and important organ in the human body and it is composed of about hundreds of billions of neurons connected by trillions of synapses. Countless electro-chemical reactions happening in those neurons every second. The reactions produce our thoughts, memory, movement, and the way we feel the physical world.

The human brain works like a CPU of a computer. It processes signal and information received from all kinds of devices (eyes or ears) and send the commands back to execution units (hands or legs). But the human brain is more powerful than a computer. Humans created art, literature and solved countless problems in science with their brains. But more important is, the brains give us a high level of cognitive ability and that make us keep searching for the answer of the ultimate question of life, the universe, and

everything (probably not 42).

In the early days of brain research, most of the interest was focused on the structure of the organ. Then researchers discovered that there is a connection between biological structure and function. Even though some considerable scientific progresses have been made, but we are far from understanding how our brain works.

With the development of technology, more and more new technique will be used in brain research to benefit the whole human beings. So in this study, I aim to develop and improve the brain activity measurement system based on the highly sensitive MI sensor and hope to provide a new choice for diagnosing brain functional disease or helping people in health care area in the future.

1.2 Theory of Brain Electromagnetic Activity

As the source of all our thoughts, emotions and behaviours, the communication between neurons play a very important role in our brains. Figure 1.1 shows the structure of a typical neuron in the central nervous system[1]. A neuron is an electrically excitable cell that processes and transmits information through electrical and chemical signals. On one end of a neuron, there are branched structures called dendrites for receiving signals from other neurons. On the other direction, a long cable-like structure called axon strerches away and branches to multiple terminals for sending signals. These terminals connect with the dendrites of other neurons (not physically

touch), also known as synapses, to accomplish the signal delivery.

The brain's electrical charge is maintained by billions of neurons which are constantly exchanging ions with the extracellular milieu. Brainwaves are produced by synchronised electrical pulses from masses of neurons communicating with each other. The electric potential generated by an individual neuron is far too small to be picked up by EEG or MEG. Usually brain activity always reflects the summation of the synchronous activity of thousands or millions of neurons that have similar spatial orientation.

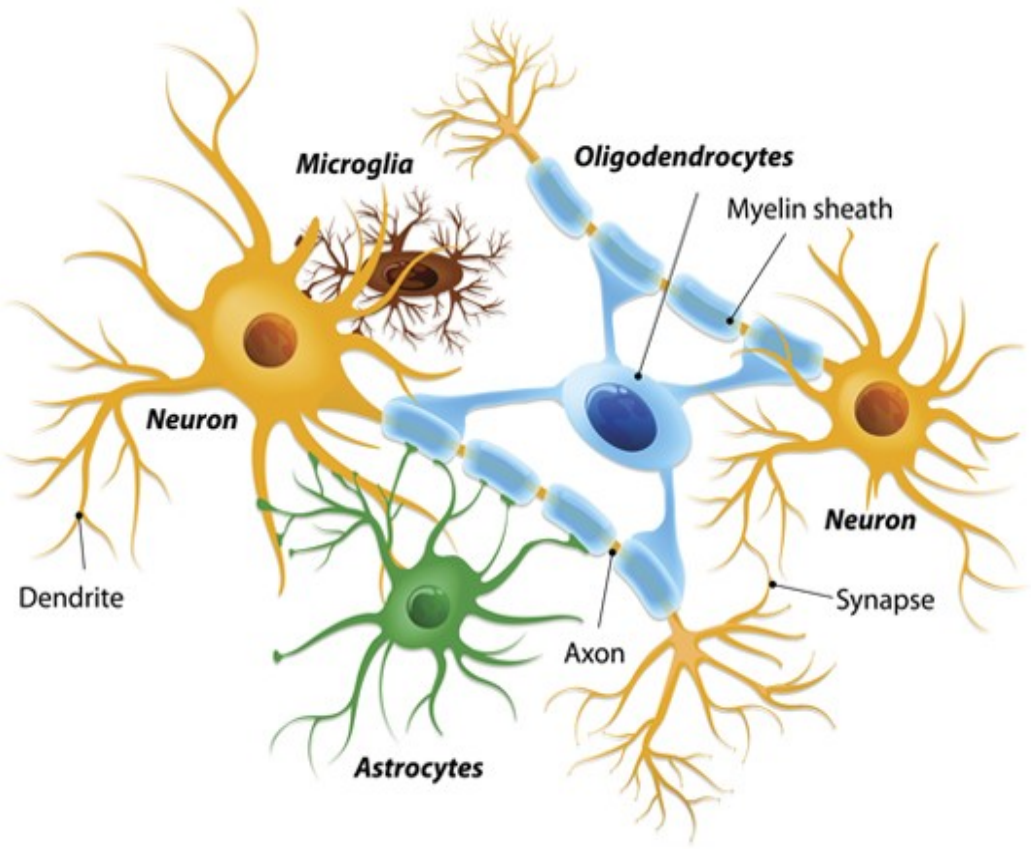

Figure 1.1 Structure of a typical neuron of the central nervous system [1]

1.3 Applications for Brain Activity Measurement

Advance in structural and functional research of brain gave us a more profound understanding of our brains in the past few decades and more and more programs are committed to research in this field. In medical & healthcare area, analyzing the brain signals can be helpful in diagnosing some diseases like epilepsy and dementia[2], detecting neural damage, tumors, coma, sleep disorders, brain death, and preventing a crash if the driver fall asleep.

And in engineering area, the Brain Computer Interfacing (BCI) technology based on real-time brain signal processing, also contributed in a lot of fields. The BCI is an amazing tool used in interaction between a human and a machine but without any muscle action[3]. It could be very useful as an assistive device for people with disabilities. For example, people who lost motor functionality can control a robotic arm or a wheelchair only by their minds[4,5]. This technology can also have wide applications for healthy user, like playing a toy helicopter using your mind instead of a gamepad[6].

1.4 Conventional Methods for Measuring Brain Activity

Many useful methods are created and improved to monitor and measure the brain activity. As the key technology, they play the most important roles in medical diagnosis and neuroscience research. Even though some of them have a quite high maintenance cost and limited in specific experimental

environment, they can provide valuable and accurate data.

Of these methods, some of them, such as Magnetic Resonance Imaging (MRI) and Computed Tomography (CT), are used to perform structural analysis. They analyze the anatomical properties of the brain to find structural deviations like tumors, thrombus, hemorrhages and deficits in infants. There are some other methods for proforming functional analysis, which aimed to measure brain activity and locate the region related. Positron Emission Tomography (PET), Electroencephalography (EEG), Magnetoencephalography (MEG) and functional Magnetic Resonance Imaging (fMRI) are the most versatile functional analysis solutions. They are useful for diagnosing epileptic seizures or diseases affecting. Also functional imaging is used to locate the functional cortex to guide the best approach in surgical treatment.

1.4.1 Computed Tomography (CT)

Computed Tomography (CT), also known as Computerized Axial Tomography (CAT), is a method used to visualize the brain and detect the intracranial abnormalities without removing any bone flap from the skull. The technology was invented by a British engineer named Godfrey Hounsfield and a South Africa born physicist named Allan Cormack in 1970s. With over 40 years development, the CT has been proved that it is a very useful diagnostic tool in multiple areas and it has made remarkable improvements, including image quality, resolution and scan speed.

Like all typical X-rays, the patient will be exposed to a small amount of radiation during the CT scaning. A CT scan combines several of X-ray images taken from different angles and uses computer processing to create cross-sectional images of internal structure of our bodies like bones, organs or blood vessels. During the scaning, patient lies down on a table inside a ring-shape gantry. Within this gantry is the X-ray source and the detector. The X-ray source moves around the patient and the detector, set up opposite the X-ray source, measures the radiation dose passes through the bones or tissues. Then the image is reconstructed by the computer for immediate evaluation.

Comparing with conventional X-rays, the resolution of CT is much better and the images provide more detailed informations. Furthermore the CT scan has a very low risk, the biggest potential risk is from radiocontrast agents. Depending on the scan type, a radiocontrast agent will be injected into the blood vessels of patient or orally administered before the procedure. It will help to distinguish normal tissues from abnormal tissues or blood vessels from other structures. However, someone may have adverse reactions to those radiocontrast agents, including nausea, vomiting or urticaria, and very few people can have a serious allergic reaction[7]. Besides those unusual reactions, it may cause kidney damage for a few of patients particularly if they already have kidney disease. After the scaning, the patients are usually advised to drink lots of water to help flush their kidneys removing the radiocontrast agents.

1.4.2 Magnetic Resonance Imaging (MRI)

Magnetic Resonance Imaging (MRI), invented by an American physician named Raymond Damadian in 1977, is a medical imaging technique developed from Nuclear Magnetic Resonance (NMR). Unlike the CT, MRI is a noninvasive imaging technique th • at produces two dimensional or three dimensional detailed anatomical images without using any X-ray sources. That makes the MRI a better choice when frequent scaning is required, especially in diagnosing aneurysms or tumors in brain. Unfortunately it is more expensive than CT scan. MRI is also widely used to image spine to evaluate the bone marrow, cardiac morphology and shoulder/knee injuries.

MRI uses properties of protons (hydrogen atoms), which abundant in water or lipids that make up over 70% of human body. The magnets used in MRI are extremely powerful. They can produce a strong magnetic field that force the protons in the patient body align with that magnetic field[8]. Then a radiofrequency pulse is turn on and force protons into a 90 or 180 degree realignment. When the radiofrequency pulse is turn off, the protons return to the normal spin and the process release electromagnetic energy. The MRI device can detect the energy change and distinguish the types of tissues, depend on the time of energy release after the radiofrequency pulse is turned off.

The potential risks in a MRI are existing. As with CT scan, during an MRI scan, the patient needs to lie on a movable table which can slide into a enclosed tunnel. Even though the patient will not feel the magnetic field or radiofrequency pulse, there may be a lot of loud noise and the patient is often

given a special ear protection. Also the entire proceduce usually need about 30-60 minutes and sometime it may be very difficult for the patients who have claustrophobia or for young children. The most dangerous thing in an MRI scan is having any metal object that contains iron and easily be magnetized or ferromagnetic in the room or in the human body. Furthermore, there is other risks, include magnetic field interference with biomedical implants such as a pacemaker or ocular prostheses. The magnetic field could affect the functioning of the device or cause it to dislodge within the tissue.

1.4.3 Positron Emission Tomography (PET)

Positron Emission Tomography (PET) is also a type of diagnostic radiology technique which produces three dimensional images of functional processes in the body. The technique was developed in the 1970s and wildly used in the oncology, neuroimaging and cardiology field. As the PET can image physiologic or biochemical phenomena, a combination with CT, called PET-CT, has become the primary diagnosis tool for obtaining both anatomic and metabolic information in one examination.

Before a PET scan, a small amount of specially designed radioactive molecules, also called tracers, need to be administered to the patient by intravenous injection. They are made up of chemical substances like sugars and proteins, which used by the particular organ or tissue during the metabolic process, attaching radioactive isotopes with short half-life such as nitrogen-13 and fluorine-18. A sugar called Fluorodeoxyglucose (FDG), which

labeled with fluorine-18, is the most commonly used tracer in PET scan.

After the waiting period that the tracer concentrated in the target tissues, the patient will be placed on a moveable table and slide into the scanner (like CT and MRI). The decay of the radioactive isotopes produce a kind of particle called positron, which like an electron but oppositely charged. When a positron interact with a surrounding electron, they annihilate each other and produce two photons moving in opposite directions. The detectors set around the suject measure these photons for reconstructing images of how the internal organs work.

As with the CT scan, except allergic to tracer, the risk of PET is quite low. Because the half-lives of isotopes used in the tracer are very short, normally from minutes to hours, the radiation dose conferred to a patient is very small. However, it makes the tracer very short-lift and can not be saved for a long time. Mostly the tracers have to be built fresh using a cyclotron near by the PET facility.

1.4.4 functional Magnetic Resonance Imaging (fMRI)

Functional Magnetic Resonance Imaging (fMRI), developed in 1990s, is a technique for measuring and mapping brain activity noninvasively. Even though the concept is built on the traditional MRI technology, the fMRI is used to focus on functions rather than only structures. fMRI is a remarkable tool to help us understand how our brains work and how the the normal functiuons of our brains are disrupted in diseases by more and more

researches.

The most common method a fMRI used is measuring the oxygen consumption of different area of brain. It is called Blood-Oxygen-Level Dependent imaging, or BOLD. When a brain area is active, the neurons in that area will consume more oxygen to maintain the biochemical reactions than usual. As oxygen is delivered by hemoglobin in capillary red blood cells, the local blood flow to that area will increase when neural activity happened. Hemoglobin is diamagnetic when carrying oxygen but becomes paramagnetic when the oxygen depleted. The difference of magnetic properties between them can be detected by a fMRI device and used to map the actived brain area.

1.4.5 Electroencephalogram (EEG)

Electroencephalogram (EEG) has a very long history as a method to evaluate the brain functions by measuring the electrical activity of neurons on the outer layer of the brain. It can measure and monitor the change of the brain activity at different spots of the head simultaneously and plot a two dimensional map of the cerebral cortex activity. The technique was invented in 1924 by a German psychiatrist named Hans Berger. With decades of development, EEG has been proved that as a safe and relatively cheap method, it can produce very accurate data with millisecond temporal resolution. In medical area, it has been widely used in diagnosing epilepsy, tumor, coma, degenerative diseases, brain death and other brain functional

research. Besides its low cost, the other advantage of EEG is convenient. The device is quite portable and tolerant of subject movement, which can be a valuable tool in BCI applications. Some of the EEG systems even could be integrated into a wearable gear. That makes the brain activity can be measured and monitored in a easier way.

In a conventional EEG task, a multiple-electrode system, which could have about 4 to 256 electrods, is used to records the electrical signals of neurons at different spots. The subject normally will be asked to wash his/her hair before the procedure in order to remove the dead skin cells for reducing the impedance. Sensitive electrodes will be attached to the subject's scalp with a conductive gel or paste to make a better contact. Then the EEG device will recode the electrical signals by electrods, amplify them and give a graph of electrical potential versus time.

Normally the EEG is a safe and painless method to measure brain activity, but in order to obtain a better spatial resolution and signal-to-noise ratio (S/N ratio), a method called intracanial EEG (iEEG) or Electrocorticography (ECoG) was invented. It is an invasive procedure which need a surgery to remove a part of subject's skull and implant the electrodes into the cortex directly.

1.4.6 Magnetoencephalogram (MEG)

Magnetoencephalogram (MEG) is also a non-invasive technique for mapping and evaluating the functional activity of brain. Unlike EEG, MEG

measurs the magnetic field produced by the ionic current of activited neurons. Even though EEG and MEG measure the signals produced by the same neurophysiological processes[9], as the skull and scalp are not very good conductors, magnetic field change is less distorted than voltage change measured by EEG, which result in a better spatial resolution of the MEG. By analyzing the spatial distributions of the magnetic field measured by MEG can also help to localize the signal source of brain activity. Furthermore, MEG is much quieter than fMRI, and it barely make any operational noise during the task. This makes the MEG a better choice on brain activity research of sleeping, auditory functions and for young children.

The magnetic field produced by neurons of brain is extremely weak. It is commonly measured by a sensitive device called Superconducting Quantum Interference Device, or SQUID. However, in order to maintain the superconductivity during the measurement, the sensor heads need to be cooled at a very low temperature, which usually uses liquid nitrogen (-195.79℃/ 77K) or liquid helium (-269℃/ 4.2K). Also because of the extremely high sensitivity of SQUID, it needs to be set up in a magnetically shielded room to eliminate the external noise. It makes the device large-scale and inconvenient.

1.5 Magnetic Field Sensors

The magnetic field sensors are solid state devices that wildly used in all kinds of applications, such as read head in HDD[10], position or navigation sensing[11] and biomagnetic field detection[12].

1.5.1 Hall Effect Sensor

A Hall effect sensor is a kind of device that convert the external magnetic field to voltage signals. It is invented based on the theory of the Hall effect, named after the American physicist Edwin Hall who discovered the phenomenon in 1879. Hall effect sensors are inexpensive and have simple structure, which make them available for wide applications, like rotary speed sensors for vehicles or sensing presence of magnetic objects in industrial productions.

As shown in figure 1.2 (a), a Hall effect sensor is constructed from a rectangular thin sheet of p-type semiconductor material, such as gallium arsenide (GaAs) or indium arsenide (InAs). The output is set perpendicular to the direction of the continuous current. When a magnetic field with a perpendicular component is applied on the semiconductor sheet, as shown in figure 1.2 (b), it will deflect the charge carriers due to the Lorentz force. As the electrons move to a side and holes move to the oppoite side, a potential difference, will be generated between the two sides. Then by measuring the potential difference, also known as Hall Voltage, the magnetic field could be

computed. The output Hall voltage is given as:

$$V_H = \frac{R_H}{d} IB \tag{1.1}$$

Where V_H is the Hall voltage, R_H is the Hall effect coefficient, I is the current flow through the Hall effect sensor, d is the thickness of the semiconductor sheet and B is the magnetic flux density.

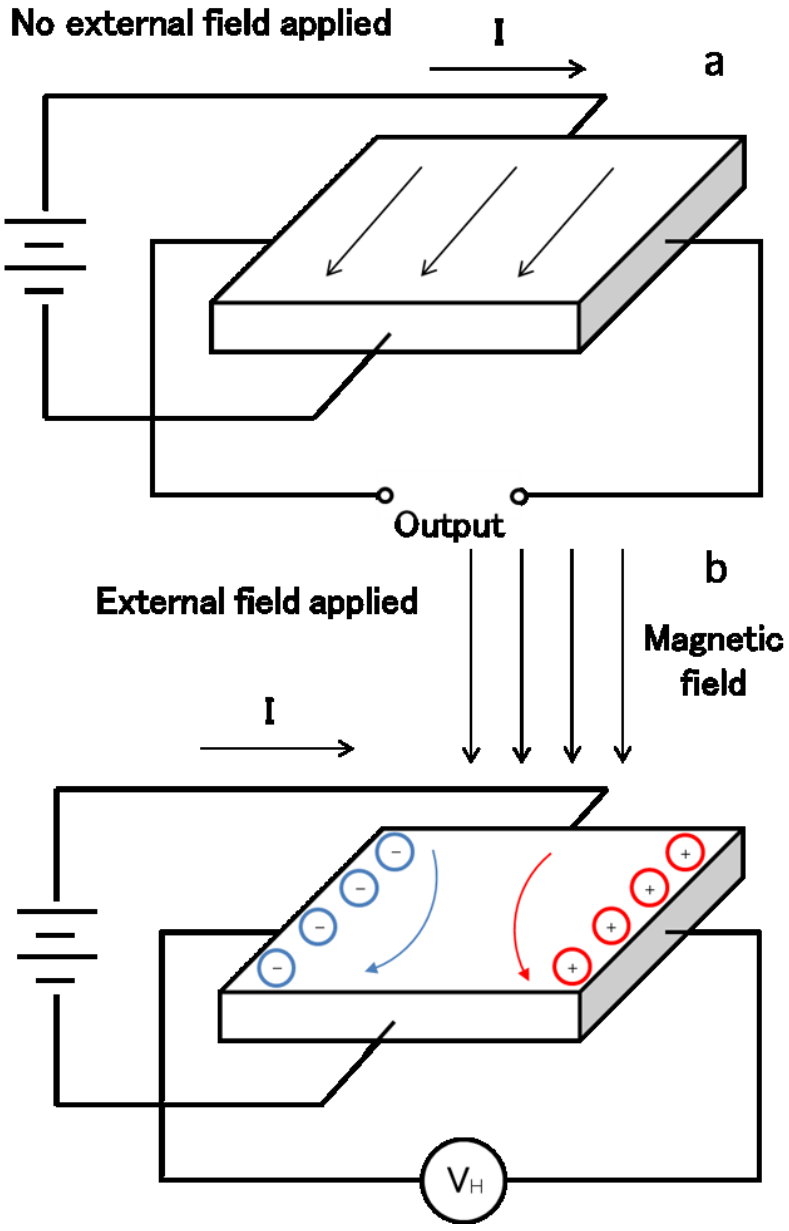

Figure 1.2 Basic principle of a hall effect sensor.

1.5.2 Magnetoresistive Sensor

The Magnetoresistive (MR) effect is a phenomenon that the electrical resistance of a material change caused by an externally applied magnetic field. The ordinary magnetoresistive (OMR) effect was first discovered by William Thomson, also well known as Lord Kelvin, in 1856. As with the Hall effect, based on the Lorentz force, the current is deflected due to the applied external magnetic field and it leads the increase of current path, thus, an increase of the effective resistance. Because of the low MR ratio (resistance change at room temperature and low magnetic field), the applications are very limited.

Later in 1857, William Thomson discovered the Anisotropic MR (AMR) effect. The AMR effect is the property that the electrical resistance of a material depends on the relative angle between the electrical current and the magnetization direction, typically in ferromagnetic materials. Figure 1.3 (a) shows a basic schematic of the AMR effect. The resistance is given as:

$$R = R_0 + \Delta R_0 cos^2\theta \qquad (1.2)$$

Where R_0 is the resistance without application of external magnetic field, ΔR_0 is the change due to the AMR effect and the θ is the angle between current and magnetization direction.

An AMR sensor is usually constructed of thin films of Permalloy (nickel-iron magnetic alloy) with stripes of aluminum or gold placed at an angle of 45°on it. The current flows along the shortest path in the high resistivity gaps thus the current is forced to flow in a direction of 45◦ respect to the magnetic field[13] as shown in figure 1.3 (b). It is called the

barber-pole configuration. The AMR sensors are widely used in rotation and position detection in smartphones and laptops. They are also used for measuring the geomagnetic field, as electronic compasses.

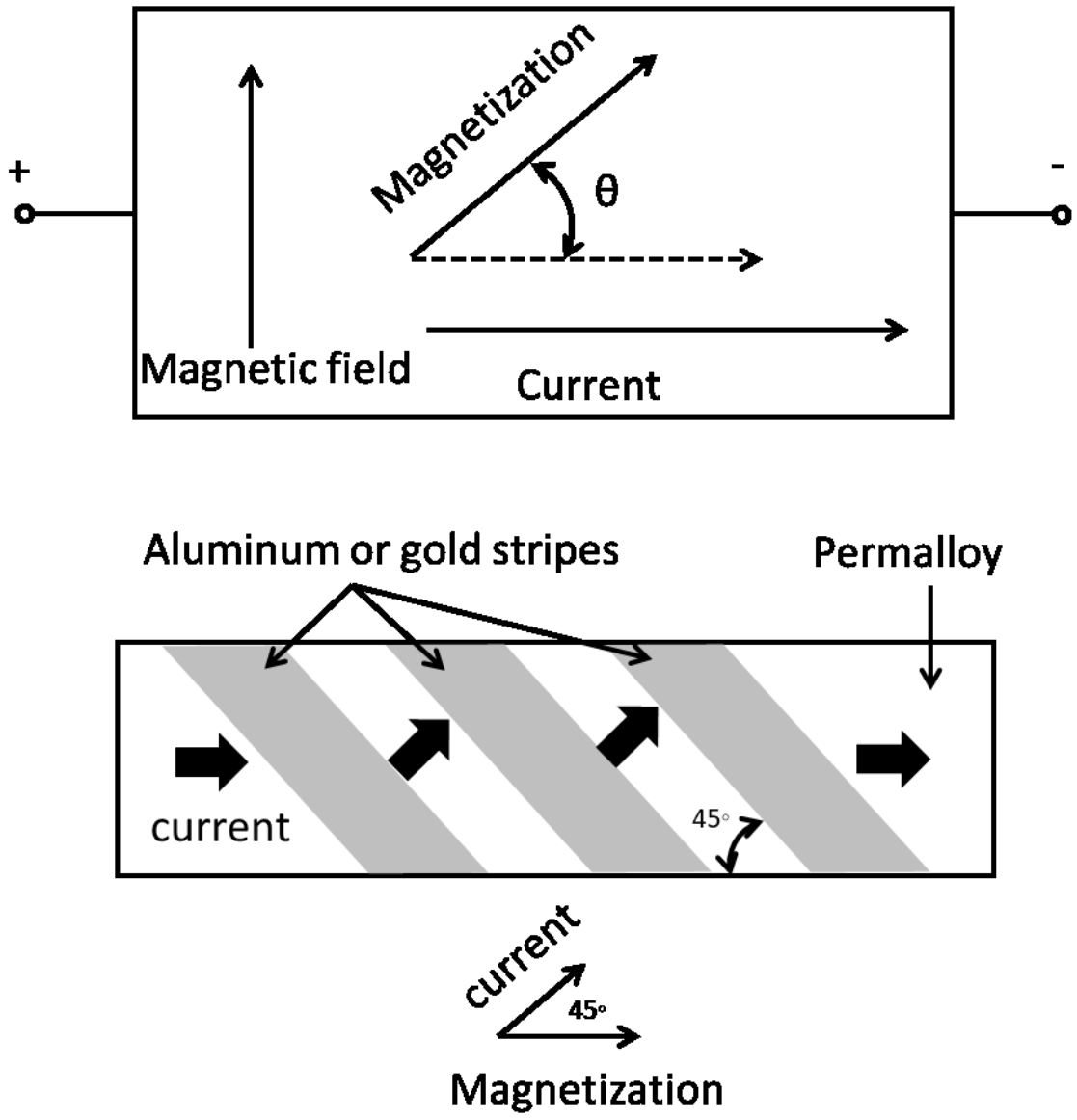

Figure 1.3 (a) A basic schematic of the Anisotropic Magnetoresistive effect. (b) The barber-pole configuration of a AMR sensor.

1.5.3 Giant Magnetoresistive Sensor

The Giant Magnetoresistive (GMR) effect is a quantum mechanical MR effect observed in thin film structures constructed of alternating ferromagnetic and non-magnetic conductive layers. It was discovered in 1988 by a German physicist, Peter Grünberg, and a French physicist, Albert Fert. As the MR ratio in GMR effect is much larger than either OMR or AMR, therefore it is called "Giant Magnetoresistance". The main application for GMR sensors are reading data in hard disk drives. They also used in magnetoresistive random access memories (MRAM).

The GMR effect is descriped as a significant change in the resistance of multi-layers when an external magnetic field changes the magnetization of the ferromagnetic layers relative to each other. Figure 1.4 shows a ferromagnetic/ non-magnetic/ ferromagnetic (FM/NM/FM) structure of GMR. In the absence of a magnetic field (left), the magnetization directions of those two FM layers are anti-parallel. In the presence of a magnetic field (on the right), the magnetization directions are parallel. The current through the FM layer is composed of two types electrons, spin-up and spin-down, and they have different scattering rates depending on the direction of magnetization. The scattering is weakest when the directions of magnetization are parallel and strongest when they are anti-parallel. As the scattering will lead a rise to extra resistance, the resistance gets maximum value when the directions are anti-parallel, and gets minimum value when the magnetization directions are parallel. The MR ratio can be defined as:

$$\frac{\Delta R}{R} = \frac{R_{AP} - R_P}{R_P} \quad (1.3)$$

Where R_{AP} is the resistance in the anti-parallel configuration and the R_P is the resistance in the parallel configuration.

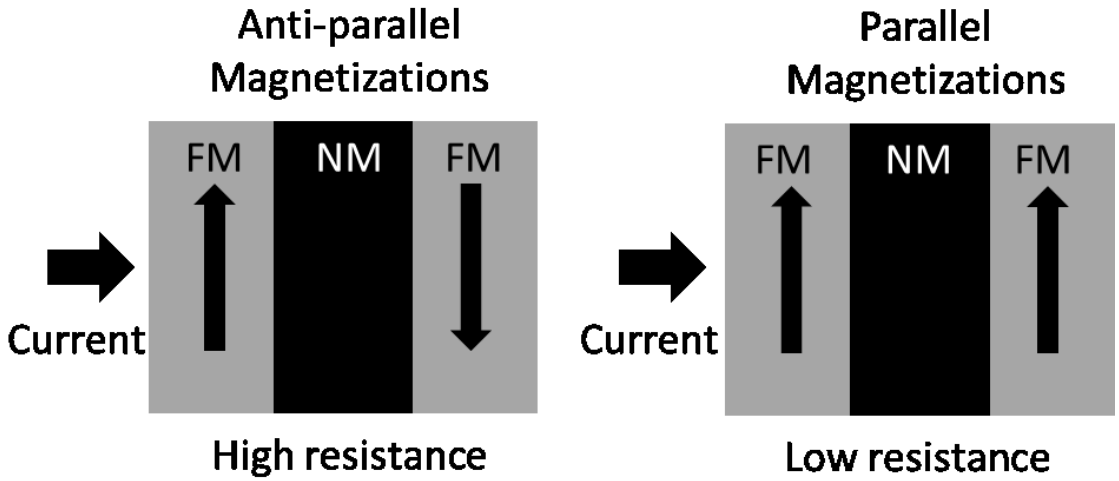

Figure 1.4 A FM/ NM/ FM structure of GMR sensor.

1.5.4 Fluxgate Magnetometer

A Fluxgate magnetometer is a highly sensitive magnetic field sensor used to measure the intensity and orientation of magnetic flux density. It was invented by H. Aschenbrenner and G. Goubau with the goal of detecting submarines in 1936 before the World War II. Now Fluxgate magnetometers have been used in many applications of industry productions and academic researches because of their favorable properties and reasonable price. They also can be used in space, such as analyzing and monitoring the magnetic fields of the earth and other planets or aerospace naviation.

As shown in figure 1.5, a basic fluxgate magnetometer consists of a

ferromagnetic core within a drive coil and a sense coil. When an AC current is applied to the drive coil, the ferromagnetic core will be driven into saturation in the positive direction, back out of saturation, and saturation in negative direction. As change of state between positive and negative saturation will change magnetic flux in the ferromagnetic core, the sense coil will detect the change and give rise to induced voltage. If there is no external field, the magnetic flux change in the ferromagnetic core will only caused by the drive coil. If there is an external field applied along the core axis, the times of those two state (saturation in the positive or negative direction) will change, one will increase and the other reduce. It will lead to shifts of the voltage induced in the sense coil. Then by detecting and measuring the magnitude of those shifts, the external magnetic field flux density could be dirived. The basic fluxgate magnetometer uses single core, in order to cancel the large signal generated by the excitation coil, double rod core and ring core are normally used[14].

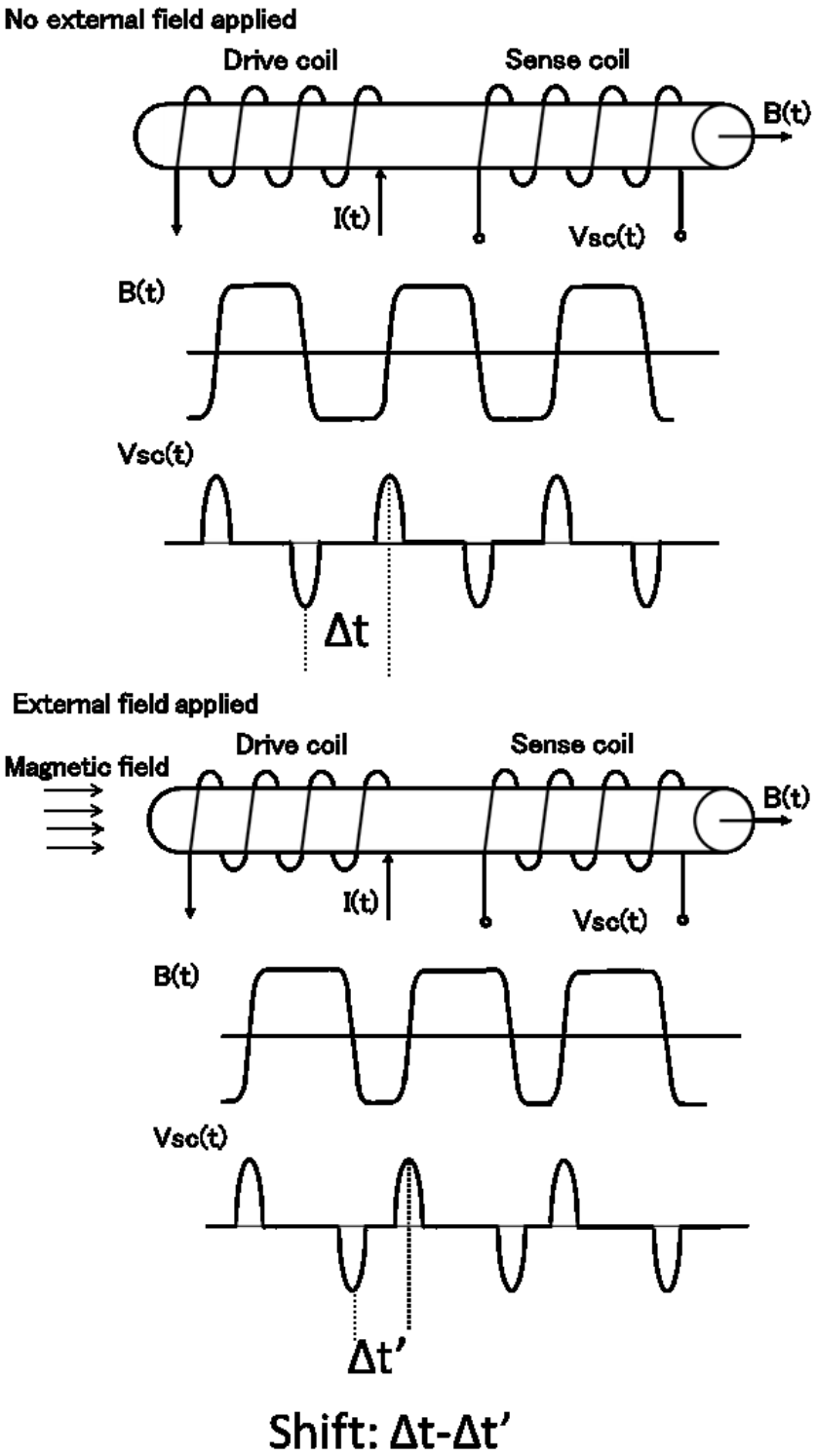

Figure 1.5 A basic principle of fluxgate magnetometer

1.5.5 Superconducting Quantum Interference Devices

A Superconducting quantum interference device (SQUID) is an extremely sensitive magnetometer constructed of a superconducting loop containing one or more Josephson junctions. It was invented in the mid 1960s soon after the first Josephson junction was made. SQUID can measure weak magnetic fields as low as fT level (10^{-15}T). Due to the remarkable sensitivity and both high temporal and spatial resolution, SQUID is widely used in ultrasensitivite magnetic measurements which the extremely weak signals can not be detected by other conventional instruments, such as brain magnetic fields in MEG or heart magnetic fields in MCG (Magnetocardiography). There are two main types of SQUID, the radio frequency SUQID (rf-SQUID) containing only one Josephson junction, and the direct current SQUID (dc-SQUID) with multiple Josephson junctions. The dc-SQUID is more expensive in construction but more sensitive than the rf-SQUID.

The basic theory of a SQUID is based on flux quantization in superconducting loop and the Josephson effect. When materials, such as niobium used in SQUID, are cooled below a superconducting transition temperature, the materials will be turned into superconductors and zero resistance. Figure 1.6 shows a basic schematic of a dc-SQUID. The core element is a ring of superconducting material with two Josephson junctions in parallel. A constant biasing current I is applied to the ring. In the absence of any external magnetic field, the current will divides equally between those two Josephson junctions, $I_1=I_2=I/2$, and no voltage is detected. Each

Josephson junction has a critical current I_c. Based on Josephson effect, a voltage appears when the current passed through a Josephson junction exceeds critical current I_c. The critical current of the SQUID is two times critical current of the junction. When a magnetic field is applied perpendicular to the plane of the ring , it will cause an internal magnetic flux Φ within the ring and the ring responds with a screening current I_s to satisfy the requirement of flux quantization. The flux through the ring can only be taken on values that integer multiples of a basic flux quantum Φ_0:

$$\Phi + LI_s = n\Phi_0 \tag{1.4}$$

$$\Phi_0 = \frac{\hbar}{2e} \approx 2.067833 \times 10^{-15} Wb \tag{1.5}$$

Where L is the inductance of the ring, and Φ_0 is one flux quantum, $\hbar$ is Plank's constant, 2e is the charge of the Cooper pair of electrons. The screening current I_s, which change direction every time the flux increases by half integer multiples of flux quantum, equals $\pm(\Phi_0/2L)$ when applied magnetic flux Φ is $(n+1/2)\Phi_0$ and equals zero when applied flux Φ is $n\Phi_0$. Due to the screening current, the critical current of the SQUID is reduced to $2I_c - 2I_s$, therefore, the critical current of the SQUID becomes a periodic function of the applied magnetic flux. If the biasing current slightly larger than $2I_c$, then the SQUID always operates in the resistive mode. The output voltage is a periodic function of the applied magnetic flux.

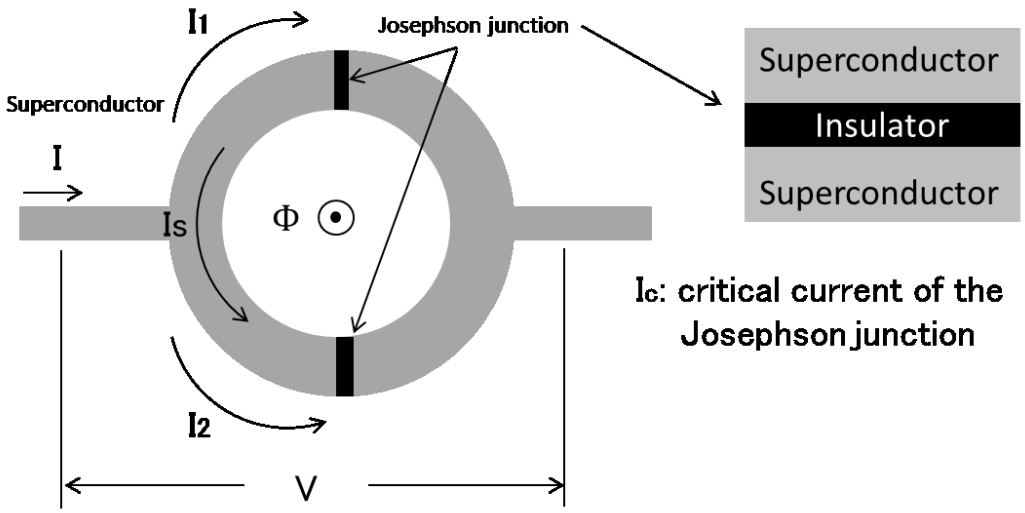

Figure 1.6 A basic schematic of a dc-SQUID

1.6 Measurement Positions of Brain Activity

There are many kinds of brain activities and all of them have their unique characteristics. One of those characteristics is their signal sources could be very different when the activity occurring, thus measurement on different position could obtain very different results. The International 10-20 system is used to describe the location of scalp for placing EEG electrodes. It is based on the landmarks of the human skull, the nasion, inion and the left and right preauricular points[45]. The system is named "10" and "20" because the distance of two adjacent electrodes between nasion and inion or the left and right preauricular points are set a serius as 10%, 20%, 20%, 20%, 20%, 10% of the front–back or left-right distance of the skull, as shown in figure 1.7. Moreover, as there are 4 major lobes of the cerebral cortex in a human brain,

including frontal, temporal, parietal and occipital lobes, the International 10-20 system uses the first letter of those lobes to represent the location, uses a number to represent the brain hemisphere, odd numbers on the left and even numbers on the right. "z" means the midline. In this study, as the number of MI sensors is very limited and all positions of the system are easy to locate, all measurement positions is chosen based on the International 10-20 system.

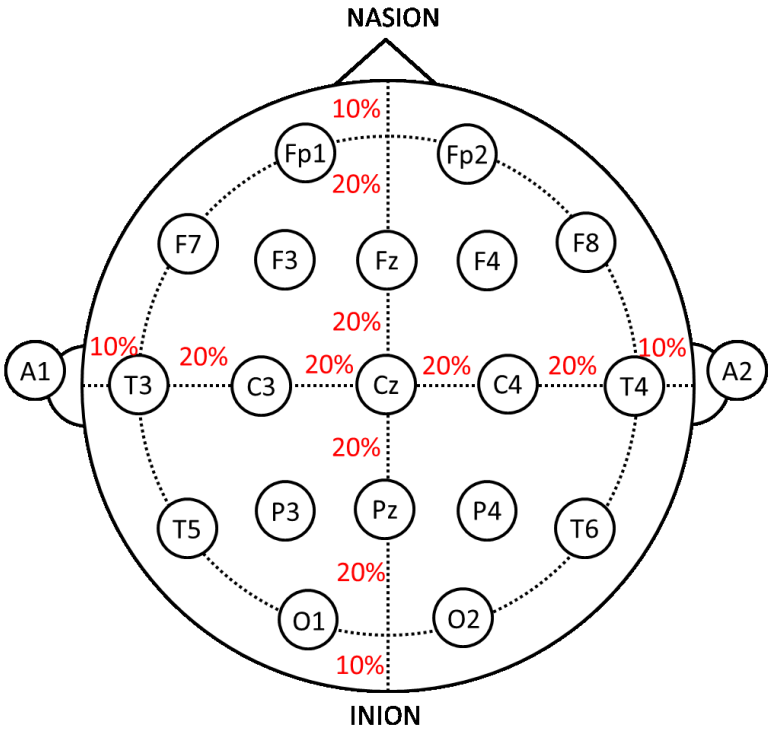

Figure 1.7 The International 10-20 system. The distances between adjacent electrodes are 10% or 20% of the nasion-inion or left-right distance.

1.7 Types of Brain Activity

The brain activity, or brain oscillations, refers to the rhythmic or repetitive activity generated by neural cells spontaneously or in response to some stimuli. They are produced by synchronised electrical pulses from masses of neurons communicating with each other. As the root of all our thoughts and behaviours, most of the research are focus on two types of brain activity, the spontaneous activity and the induced activity.

1.7.1 Spontaneous Activity

Spontaneous activity is a kind of brain activity that always fluctuating in a sustained state and not related to external stimuli. It is considered to play a important role during brain development. Spontaneous activity is also considered to be connected with the current mental state of a person, such as wakefulness or alertness, and it is usually used in sleep research. However, spontaneous activity is usually considered as noise in induced activity processing. Depanding on the different frequency bandwidths, the majority of the spontaneous activity could be signified as delta, theta, alpha and beta rhythm, as shown in figure 1.8[15]

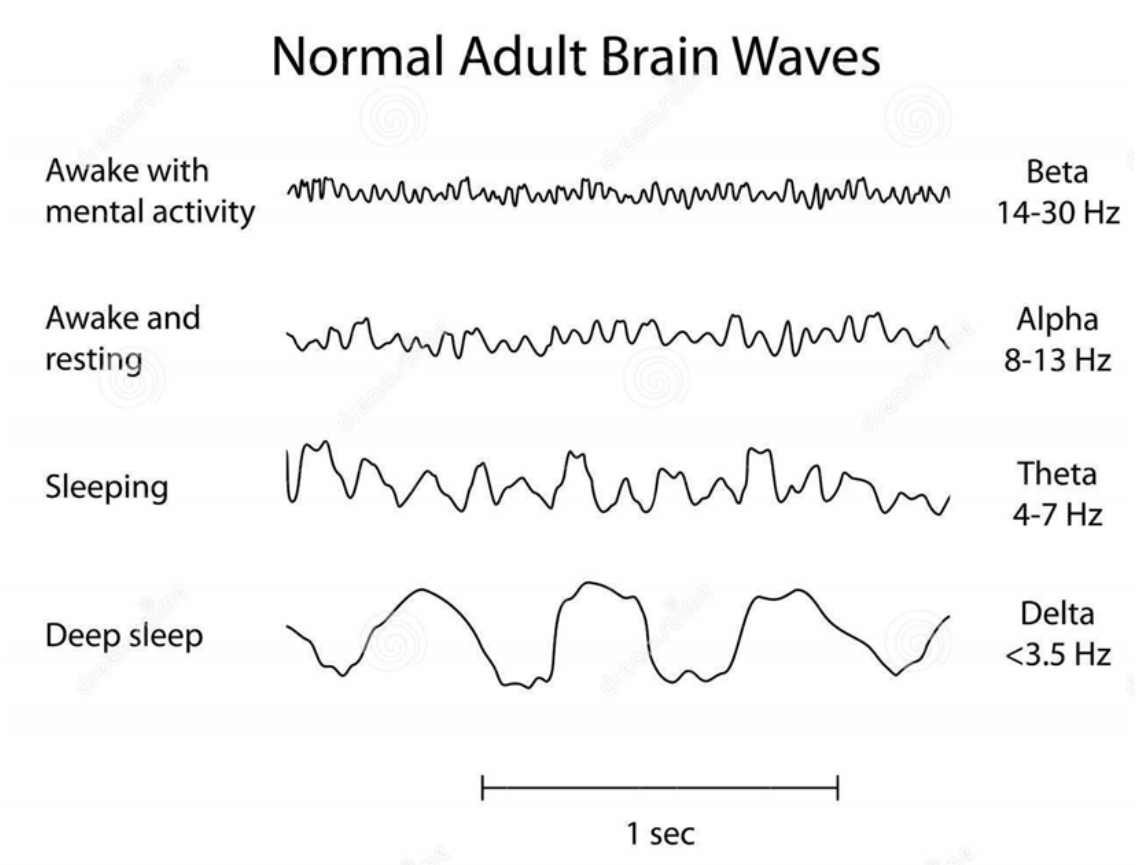

Figure 1.8 Brain activity in different frequency measured by EEG [15].

Delta rhythm

Delta rhythm tends to be the highest in amplitude but slowest brain wave with a frequency bandwidth of 0.5-4 Hz. It is normally observed in adults during their depth of sleep or in babies.

Theta rhythm

As with the delta rhythm, theta rhythm is a low frequency brain wave which in the frequency range from 4-7 Hz. It has been connected via an extensive study to many different phenomena in the brain. Research on

subjects as diverse as memory, emotion, neural plasticity, sleep, meditation and hypnosis have all drawn links to theta waves. A theta wave state is associated with stage 1 sleep, a very light sleep from which subjects can easily be awoken.

Alpha rhythm

Alpha rhythm is a neural oscillation in the frequency range of 8-13 Hz. It is generally associated with relaxed wakefulness, and commonly described as tranquil and pleasant-sometimes accompanied by a floating feeling. Alpha rhythm is also indicative of a creative state of mind where free association is prominent. Alpha rhythm appears immediately and spread throughout the cortex when you close your eyes, which is part of the relaxation process leading to sleep. It has also been connected to the ability to recall memories, lessened discomfort and pain, and reductions in stress and anxiety.

Beta rhythm

Beta rhythm is the term used to designate the frequency range of human brain activity between 13-30 Hz. It is generally the mental state most people are during the day, and usually this state in themselves is uneventful. However, beta rhythm is significant to proper mental functioning, and insufficient beta waves can cause mental or emotional disorders such as depression and insomnia. Broadly speaking, beta rhythm is associated with alert attentiveness and concentration- intense focus and problem solving are linked to beta rhythm. It can also be related to strong, excited emotions.

1.7.2 Induced Activity

Induced activity, or evoked activity, refers the brain activity induced by processing the external sensory stimulation. Opposed to the spontaneous activity, induced activity relates a task, such as a visual stimulus or a requirement of movement. Because of the weak amplitude, induced activity is easily buried by the spontaneous activity signals. Normally it needs to repeat the stimulus multiple times and average the signals to reduce the high amplitude spontaneous activity and reveals the induced activity.

Auditory Evoked Field

Auditory Evoked Field (AEF) is a neural activity induced by auditory stimuli and recorded by MEG. An equivalent called Auditory Evoked Potential (AEP) is recorded by EEG. One of the main sources of the AEF is called auditory cortex, which is a part of the temporal lobe that processes auditory information. The AEF is composed of a series of positive and negative magnetic field deflections which can be distinguished by their relative latency and polarity[16].

The earliest AEF cortical components, which is equivalent to the middle latency response (MLR) recorded by EEG, called the middle latency auditory evoked field (MLAEF). For example, M30 and M50, occurring at 30 and 50 ms after the stimulus onset. Longer latency responses after 100 ms are referred to as Auditory Event-Related Fields (AERF), such as P300 (or P3).

N100 (or N1), or N100m (M100) called in some MEG research, one of the most prominent responses in the AEF, surfaces as a negative deflection with

a latency of roughly 80 to 120 ms after the onset of a stimulus. And it is the most widely used magnetic field response clinically, such as test for abnormalities in the auditory system where verbal or behavioral responses can not be used, like individuals in coma.

Event Related Field

Event Related Field, recorded by MEG, or Event Related Potential (ERP) recorded by EEG, is brain responses that are time-lock to some event, like a sensory stimulus or recognition of a target stimulus. It is the measured brain response that is the direct result of a specific sensory, cognitive or motor event. The location of ERF source is a disputable problem that can not be exactly solved. The ERF can also be distinguished by their relative latency and polarity.

The P300 is an important component of ERF which is usually elicited in the process of decision making. It surfaces as a positive deflection with a latency of approximately 250 to 500 ms after the onset of a stimulus, but the latency is affected by some factors, such as individual differences, difficulty of task and age etc[46]. The largest amplitude of a P300 ERP is normally obtained in parietal (Pz) region. It is also reported by some research that the more attention the subject pays to the stimuli, the larger the resultant P300[47]. Since the first discovered by Sutton et al. in 1965, because of its relatively large amplitude and facile elicitation in experimental contexts[48], the P300 component has been one of the most important ERP/ERF components in investigating the selective attention and information

processing. In application level, the P300 could be helpful in such as brain injury inspection, diagnosis of neocortical epilepsy, telemedicine or cognitive functions research. And as the EEG devices are cheaper and more convenient than the MEG SQUIDs, the P300 recorded by EEG is widely used in lie detection and Brain Computer Interfacing (BCI).

1.8 Objectives of This Study

With the development during the last two decades, the MI sensor has been improved and applied in several fields, such as a electronic compass in mobile phone. Comparing with the conventional magnetic field sensor, MI sensor has a high sensitivity and a wide range of detection, which from milli-Tesla to pico-Tesla level. Also the MI sesnsor has a low power cost and compact structure and it makes the sensor could be easily integrated into other device. People in 21 century have improved their health consciousness. Even though the SQUID is still the most sensitive sensor in biomagnetic field measurement, considering the inconvenient of be cooling or the magnetic shielding room, the SQUID might not be the best choice in some fields, like applications in wearable intelligent device.

In this thesis, based on the features of MI sensor talked above, we expect to develop a novel tool to measure and detect the magnetic activity of the brain, which could be used without magnetic shielding room and no need for cooling. To achieve this goal, first I build the brain activity measurement system using highly sensitive MI sensor and measure some brain activites. Then with comparing our results to other research, the performance of this

system is improved and new functions are add on for further measurement and development. In this study, we measured 3 brain activities in 4 kinds of tasks, the N100 AEF, the P300 ERF induced by auditory stimuli, the alpha rhythm and the P300 ERF induced by visual stimuli. Moreover, the system has updated for 3 times during those measurement.

1.9 Outline of the Thesis

This thesis consists of 6 chapters and the outline is organized as follows.

Chapter 1 is mostly about the background of brain research and related technologies. Also, a introduction of the brain activites I measured in this study is presented. At last the objectives of this study shows our goal of building this system.

Chapter 2 mostly describs the princple and performance of the MI sensor I used in this study. It also shows the structure of the sensor and how does it work. At last the detection characteristics and noise level of the MI sensor is presented.

Chapter 3 presents the study about the single-channel off-line system used in N100 AEF and P300 ERF (induced by auditory stimuli) measurement, including the functions of this system, the methods we induced the brain activity, the experiment details and what can we know from the results. Chapter 3 is mainly based on a proceeding paper[17] and a journal paper[18].

Chapter 4 presents the study about the single-channel real-time system used in alpha rhythm and P300 ERF (induced by visual stimuli) measurement. The system in chapter 4 is a updated version of that in

chapter 3, which with the real-time signal processing module and integrated stimuli generator. It provides a possibility that MI sensor could be used in BCI application in the future, Chapter 4 is mainly based on a journal paper[19].

Chapter 5 presents the study about the multi-channel system used in P300 ERF (induced by visual stimuli). This multi-channel system is updated based on the system introduced in chapter 4. A Fast Independent Component Analysis (FastICA) module is used to separate the independent components, which a conventional frequency filter could not achieve that.

Chapter 6 presents the summary, the conclusions and the future work.

Chapter 2

MI Measurement System

2.1 Basic Theory of MI Sensor

The MI sensor used in this study is a novel highly sensitive micro magnetic sensor based on the Magnetoimpedance (MI) effect in amorphous wires and constituted with CMOS IC multivibrator circuits. The MI effect is a phenomenon that a large variation of the electrical impedance in some materials when an external magnetic field applied. It is associated with the skin effect in the magnetic conductor.

The first discovery of a new principle of MI effect in a 30μm diameter zero-magnetostrictive FeCoSiB amorphous wire was in 1993 by Prof. Kaneo Mohri et al[20-23]. In 1997, a CMOS IC inverter multivibrator type MI sensor based on pulse MI effect in the amorphous wire was invented[24]. Soon in 1999, a highly stable MI sensor for temperature variation introducing analog switches was developed. Then the development of an electronic compass IC chip for mobile phones using 2-axis MI sensors was made, and also the applications on biomagnetic field measurement are going on.

2.1.1 Skin Effect

The skin effect is a tendency that when high frequency AC current passing through a conductor, more current will distributed at the surface rather than the center of the conductor. It leads the current density to be the highest at the surface and decreases with the depth in the conductor.

The skin effect happens as the conductor which carrying the AC current, is immersed in its own induced magnetic field and causing the eddy current in conductor itself. According to the Lenz's law, the eddy current produce a secondary magnetic field opposed with the induced magnetic field causing by the AC current. Then as a result, extra circulating current is generated and it will cancel the current flow in the center of the conductor and increase it at the surface.

Consider a sinusoidal current passing though a homogeneous conducting half-space along x axis, as shown in figure 2.1. The angular frequency of the current is ω, μ and σ are the magnetic permeability and electrical conductivity of the material. In order to determine the distribution of current in the conductor, assuming the vector of current density is parallel to the conductor surface and it only has x compontent depending on the coordinate y, $\mathbf{J} = j_x(z)\mathbf{u}_x$, where $\mathbf{u}_x$ is an unit vector.

Analyzing from the Maxwell's equations in time-harmonic form, as it is assumed that the conductor is homogeneous, the displacement current density can be neglected:

$$\nabla \times \mathbf{E} = -\mathrm{j}\omega\mathbf{B} \tag{2.1}$$

$$\nabla \times \mathbf{H} = \mathbf{J} \tag{2.2}$$

Since $\mathbf{E}=\mathbf{J}/\sigma$ and $\mathbf{H}=\mathbf{B}/\mu$, equations (2.1) and (2.2) become:

$$\nabla \times \mathbf{J} = -\mathrm{j}\omega\sigma\mathbf{B} \tag{2.3}$$

$$\nabla \times \mathbf{B} = \mu\mathbf{J} \tag{2.4}$$

Based on the Biot-Savart law and symmetry, it follows that there is only a y compontent of the vector **B**, the equations (2.3) and (2.4) become:

$$\frac{\partial \boldsymbol{J_x}}{\partial z} = -j\omega\mu\sigma\boldsymbol{B_y} \tag{2.5}$$

$$-\frac{d\boldsymbol{B_y}}{dz} = \mu\boldsymbol{J_x} \tag{2.6}$$

From equations (2.5) and (2.6), by eliminating $\boldsymbol{B_y}$ the equation become:

$$\frac{\partial^2 \boldsymbol{J_x}}{\partial z^2} = j\omega\mu\sigma\boldsymbol{J_x} \tag{2.7}$$

This equation has a general solution as given by:

$$J_x(z) = J_1 e^{\gamma z} + J_2 e^{-\gamma z} \tag{2.8}$$

where

$$\gamma = \sqrt{j\omega\mu\sigma} = (1+j)\sqrt{\frac{\omega\mu\sigma}{2}} = (1+j)k \tag{2.9}$$

$$\mathrm{k} = \sqrt{\frac{\omega\mu\sigma}{2}} \tag{2.10}$$

For z→ ∞, the current density can not increase indefinitrly, thus, J_1=0. The current in the surface is expressed as:

$$J_x(z) = J_x(0)e^{-kz}e^{-jkz} \tag{2.11}$$

It is obviously that with increasing z, the intensity of the current density vector decreased exponentially. The penetration depth for the conductor is expressed as:

$$\delta = \frac{1}{k} = \sqrt{\frac{2}{\omega\mu\sigma}} \tag{2.12}$$

The penetration depth is also known as the skin depth.

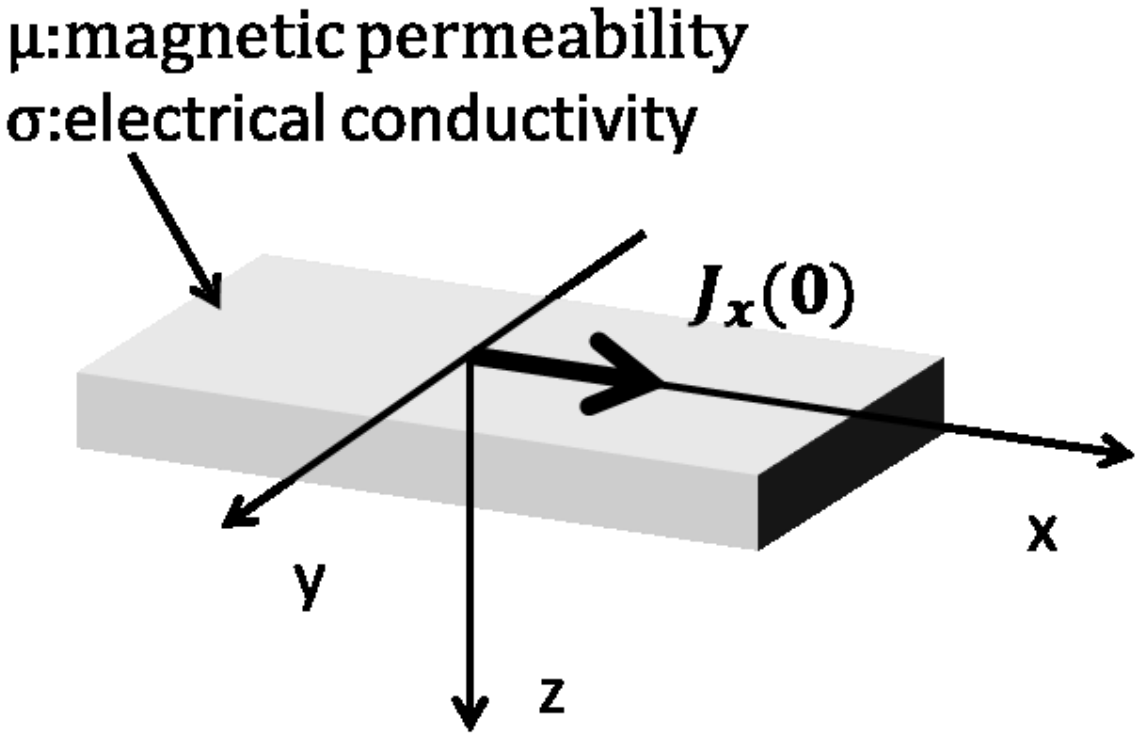

Figure 2.1 The schematic of basic skin effect in magnetic conductor.

2.1.2 Magnetoimpedance Effect

Figure 2.2 shows a basic schematic of MI effect in a cylinder (wire) magnetic material. The radius and length of the magnetic material is a and l, the electrical resistivity $\rho = 1/\sigma$. Assuming the voltage on the materral is V when a sinusoidal current $I = I_m e^{j\omega t}$ passes through it, electric field vector **E** is along the z axis, the induced magnetic field vector is **H**, and the magnetic flux density is $\mathbf{B} = \mu\mathbf{H}$.

As the Maxwell's equations are given by:

$$\nabla \times \mathbf{E} = -j\omega\mu\mathbf{H} \tag{2.13}$$

$$\nabla \times (\nabla \times \mathbf{E}) = -\mathrm{j}\frac{\omega\mu}{\rho}\mathbf{E} = \nabla(\nabla \cdot \mathrm{E}) - \Delta\mathrm{E} \qquad (2.14)$$

Since $\nabla \cdot \mathrm{E} = 0$:

$$\Delta E_z - \mathrm{j}\frac{\omega\mu}{\rho}\mathbf{E} = 0 \qquad (2.15)$$

And E_z is a function of the radial coordinate r , it is represented by cylindrical coordinates as:

$$\Delta E_z = \frac{\frac{1}{r}\partial(\frac{r\partial E_z}{\partial r})}{\partial r} \qquad (2.16)$$

Setting $-\mathrm{j}\frac{\omega\mu}{\rho} = \mathrm{k}^2$, since $\sqrt{-j} = \frac{(1-\mathrm{j})}{\sqrt{2}}$,

$$\mathrm{k} = \frac{(1-\mathrm{j})}{\delta} \qquad (2.17)$$

where $\delta = \sqrt{\frac{2}{\omega\mu\sigma}}$ is the skin depth. From equations (2.15), (2.16) and (2.17),

$$\frac{\frac{1}{r}\partial(\frac{r\partial E_z}{\partial r})}{\partial r} + k^2 E_z = 0 \qquad (218)$$

$$\frac{\partial^2 E_z}{\partial r^2} + \frac{\partial E_z}{r\partial r} + k^2 E_z = 0 \qquad (2.19)$$

Depending on Bessel's equation given by:

$$\frac{d^2y}{dx^2} + \frac{dy}{xdx} + \left(1 - \frac{\alpha^2}{x^2}\right)\mathrm{y} = 0 \qquad (2.20)$$

Denote by $J_0(x)$, the solution of the first kind Bessel functions of order $\alpha = 0$, where $\mathrm{x} = \mathrm{kr}$, E_z is expressed as:

$$\mathrm{E}_z(\mathrm{r}) = \mathrm{A}\mathrm{J}_0(kr) = \frac{E_z(a)}{J_0(ka)}J_0(kr) \qquad (2.21)$$

Where A is a constant.

Oh the other hand, $\mathrm{H(r)}$ and $E_z(a)$ are related to the current I, since

$$(\nabla \times \mathbf{E})_\phi = -\mathrm{j}\omega\mu\mathrm{H} = -\frac{\partial E_z}{\partial r} \qquad (2.22)$$

The H is expressed as:

$$\mathrm{H} = \frac{-\mathrm{j}}{\omega\mu} \cdot \frac{\partial E_z}{\partial r} \tag{2.23}$$

Then since $\partial J_0(x)/\partial \mathrm{x} = -J_0(x)$, from equation (2.21) and (2.23),

$$\mathrm{H(r)} = \frac{\mathrm{jkA}}{\omega\mu}\mathrm{J}_1(kr) \tag{2.24}$$

$$\mathrm{H(a)} = \frac{\mathrm{jkA}}{\omega\mu}\mathrm{J}_1(ka) = \frac{I}{2\pi a} \tag{2.25}$$

From equation (2.25), the constant A and $E_z(a)$ is expressed as:

$$\mathrm{A} = \frac{E_z(a)}{J_0(ka)} = -\frac{j\omega\mu I}{2\pi k a J_1(ka)} \tag{2.26}$$

$$E_z(a) = -\frac{j\omega\mu I J_0(ka)}{2\pi k a J_1(ka)} \tag{2.27}$$

The energy flux, which the energy transfer per unit area of the closed suface per unit time, is represented by the Poynting vector, $\mathbf{S} = \mathbf{E} \times \overline{\boldsymbol{H}}$ and the power $\bar{I}V$ is given by:

$$\bar{I}V = -\iint (\mathbf{E} \times \overline{\boldsymbol{H}})_n dS = E_z(a)\overline{H(a)}2\pi a l = E_z(a)l\bar{I} \tag{2.28}$$

From equation (2.27),

$$V = E_z(a)l = -\frac{j\omega\mu I J_0(ka)}{2\pi k a J_1(ka)} l \tag{2.29}$$

As the DC resistance is $\mathrm{R}_{dc} = \rho l/\pi a^2$, the impedance of the element Z is expressed as:

$$\mathrm{Z} = \frac{V}{I} = \frac{R_{dc} ka}{2} \frac{J_0(ka)}{J_1(ka)} \tag{2.30}$$

Where $\mathrm{ka} = \frac{(1-\mathrm{j})}{\delta} a$, and $\delta = \sqrt{\frac{2}{\omega\mu\sigma}}$.

In the low frequency situation, which $\delta \gg \mathrm{a}, |ka| \ll 1$,

$$\mathrm{J}_0(\mathrm{ka}) \approx 1 - \frac{1}{4}(ka)^2 \tag{2.31}$$

$$\mathrm{J}_1(\mathrm{ka}) \approx \frac{1}{2}\mathrm{ka} - \frac{1}{16}(ka)^3 \tag{2.32}$$

From equation (2.31) and (2.32),

$$\mathrm{Z} \approx R_{dc} + j\omega L_i \tag{2.33}$$

Where the $L_i = \mu l/8\pi$ is the internal inductance of the material and it is a function of μ and l. So the impedance Z in low frequency situation can be expressed as:

$$\mathrm{Z} = -\mathrm{j}\omega L_i \frac{4J_0(ka)}{kaJ_1(ka)} \tag{2.34}$$

Then in the high frequency situation, which $\delta \ll \mathrm{a}, |ka| \gg 1$,

$$\mathrm{J}_0(\mathrm{ka}) = \sqrt{(\frac{2}{\pi ka})}\cos(ka - \frac{\pi}{4}) \tag{2.35}$$

$$\mathrm{J}_1(\mathrm{ka}) = \sqrt{(\frac{2}{\pi ka})}\sin(ka - \frac{\pi}{4}) \tag{2.36}$$

From equation (2.35) and (2.36),

$$\frac{J_0(ka)}{J_1(ka)} \approx \cot\left(ka - \frac{\pi}{4}\right) \approx -J \tag{2.37}$$

The impedance Z in high frequency situation can be expressed as:

$$\mathrm{Z} \approx \frac{4\omega\delta L_i}{ka} = R_{dc}\frac{a}{2\delta} + j\omega L_i \frac{2\delta}{a} = \frac{a}{2\sqrt{2\rho}} R_{dc}(1+j)\sqrt{\omega\mu} \tag{2.38}$$

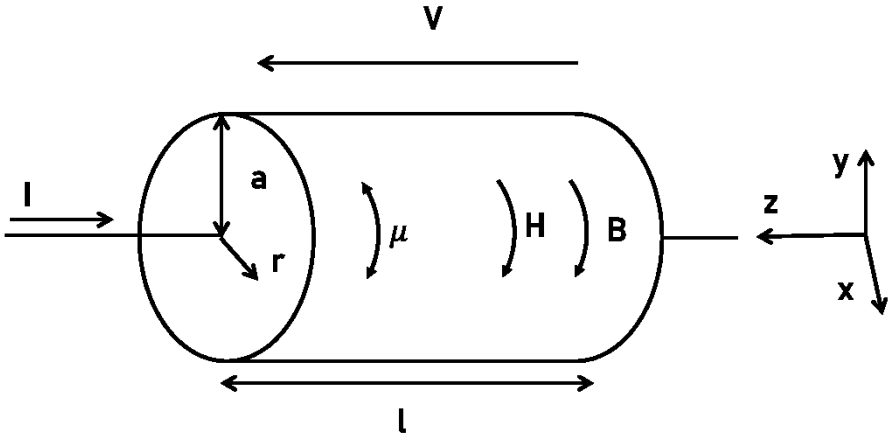

Figure 2.2 A basic schematic of MI effect in a cylinder (wire) magnetic material.

2.2 Measurement System

In this study, I built a brain activity measurement system using highly sensitive MI sensor. First the system was designed to measure and record the brain activity for off-line processing. A microcontroller is used to create the auditory stimuli for inducing brain activities (Single-channel Off-line processing system); Then the system was improved to process the brain signals faster with a real-time processing module or run the pre-processing program for later processing. And it also integrated the stimuli generate module that can produce visual or auditory stimuli (Single-channel Real-time processing system); At last, the system was updated to multi-channel for using multivariate statistic Independent Component Analysis (multi-channel real-time/off-line processing system).

2.2.1 MI Element and the Sensor Head

The magnetic field of the human brain is extremely weak, in order to measure it, we constructed a MI gradiometer that can cancel out the background noise instead of using a magnetic shielding.

The pico-Tesla resolution multi-core MI element, which provided by Aichi Steel Corporation, is shown in figure 2.3 (a). One MI element includes 4 amorphous alloy wires inside a 300 turns pick-up coil, and the noise floor of the element is lower than 1 $pT/\sqrt{Hz}$ in the frequency range from 20 to 500 Hz[25]. As shown in figure 2.3 (b), one sensor head includes two MI elements. Of the two MI elements, one is used to measure the total magnetic field (the

magnetic field of the brain, plus background magnetic noise), and the other one is used to cancel out the background magnetic noise, such as geomagnetism. As a gradiometer the voltage difference between the two MI elements are used as output, and the distance between them is 3 cm.

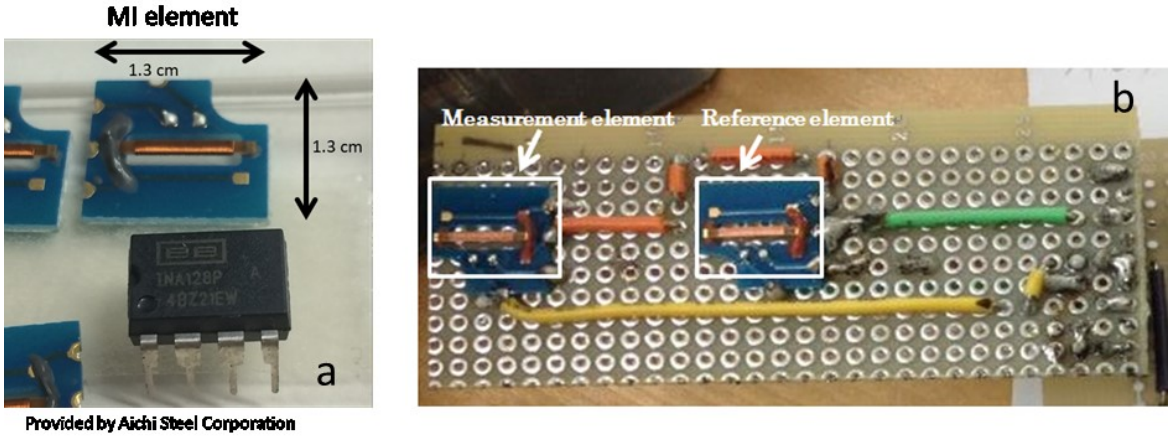

Figure 2.3 (a):Pico-Tesla resolution multi-core MI element. (b):MI sensor head, including two MI elements.

2.2.2 The Circuits of Pulse-drive MI Sensor

The measurement and analog amplifier circuits consist of basic CMOS IC. Figure 2.4 (a) shows a block diagram of one MI element circuit and figure 2.4 (b) shows the schematic diagram of the MI sensor (gradiometer). A pulse current, which has a 500 kHz oscillation frequency and a 50% duty cycle, is created by the pulse generator (part a) to excite the MI effect. Then the part b will convert the pulse current into a short-width pulse. The pulse width is set to 120 ns according to previous report[26]. The part c is designed to give a delay and convert the pulse signal into a short-width pulse. The pulse signal will control those two switches when the induced electromotive force of the

coils get the maximum value so that the sensor can obtain the maximum output. Based on previous report, the time of the delay is 20 ns and the pulse width is also 20 ns. Then the output signal will be amplified for 1000 times using a high gain analog amplifier.

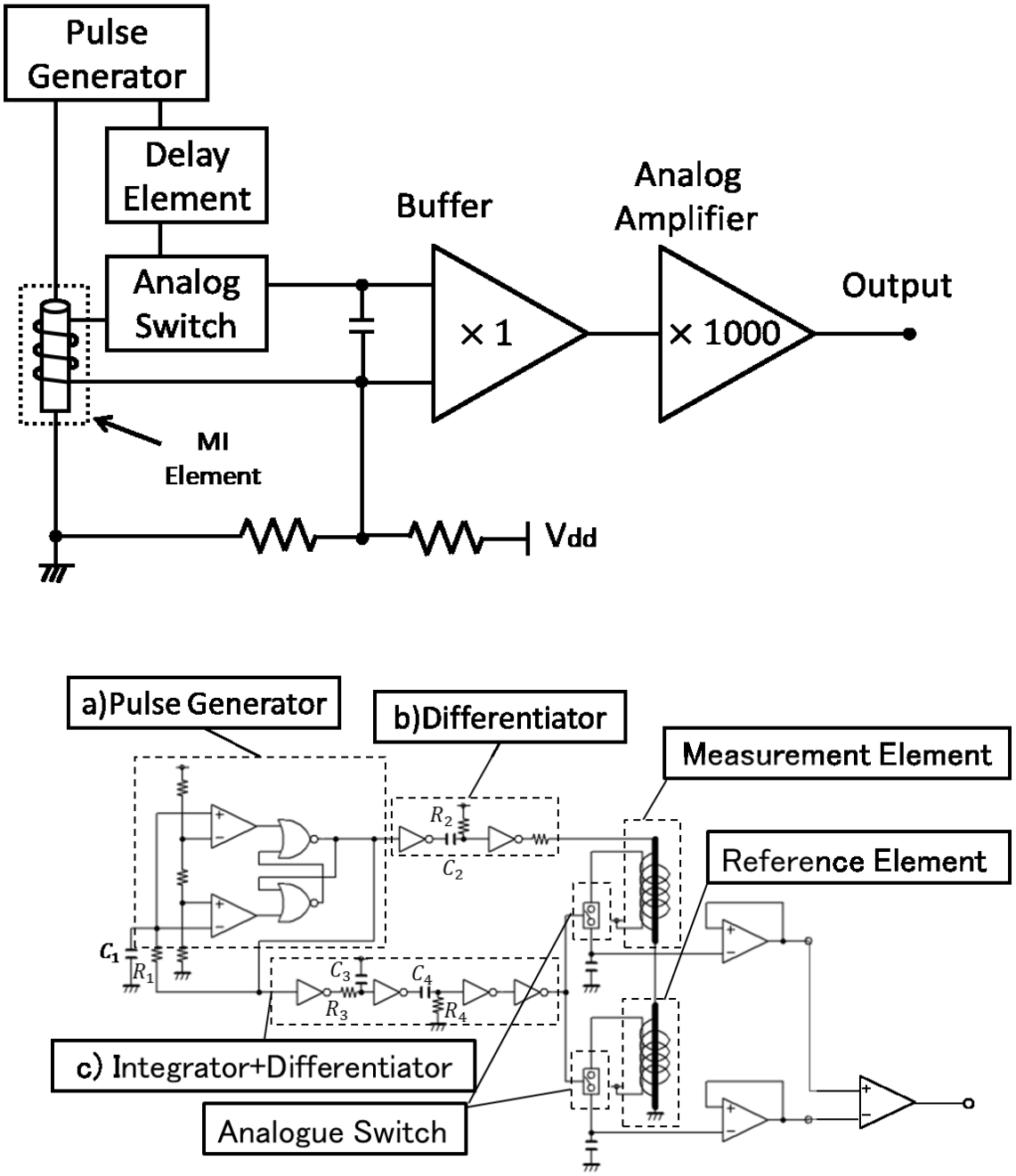

Figure 2.4 (a)Block diagram of one MI element circuit. (b)The schematic diagram of the MI gradiometer

2.2.3 Detection Characteristics of MI Sensor

The detection characteristics of both MI elements and MI sensor were measured within a triple-layer magnetic shielding box made of permalloy. The shielding effectiveness of the box is about 50 dB at 2 Hz. The DC magnetic field was applied by a Helmholtz coil. The output of sensors was recorded with the applied magnetic field increasing by a 14 bit AD converter. Figure 2.5 (a) shows the detection characteristics error of those two MI elements and in this study they are considered as the same sensitivity. Figure 2.5 (b) shows the detection characteristics of the MI sensor. It shows the linear characteristic of the MI sensor and the sensitivity is about 33kV/T.

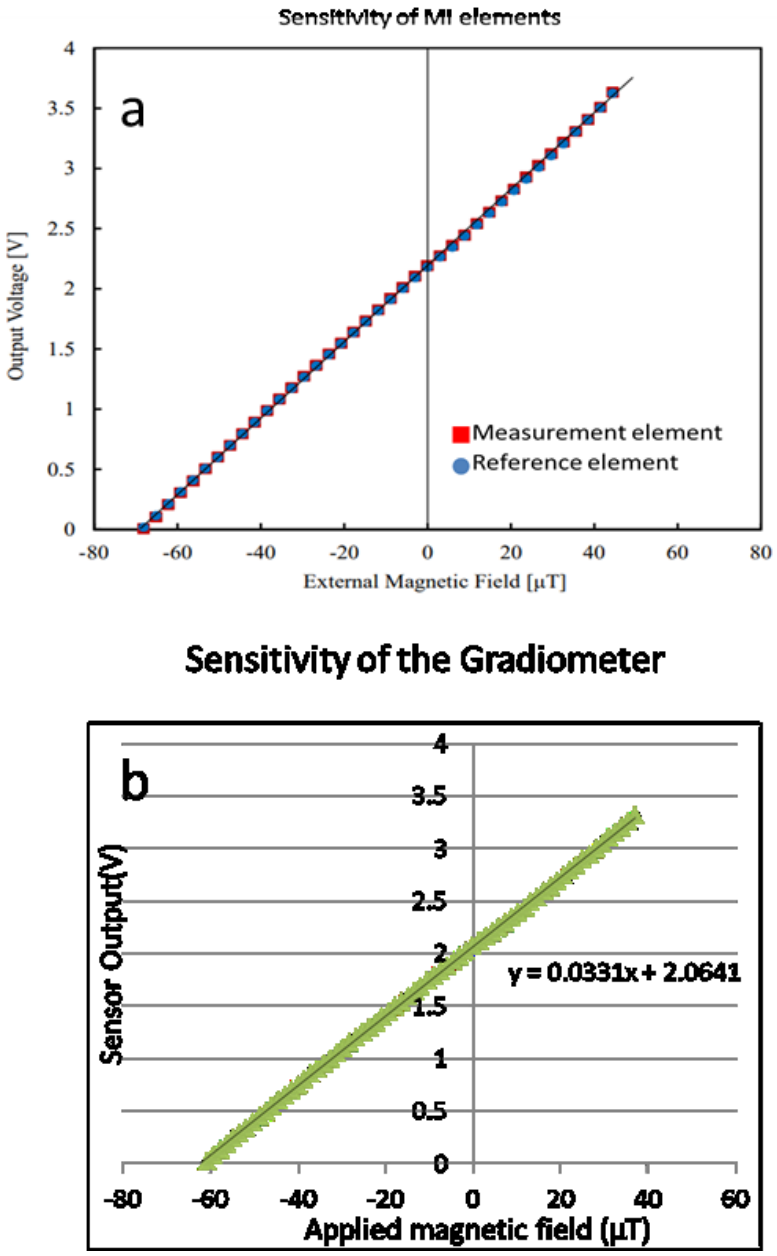

Figure 2.5 (a) Detection characteristics error of two MI elements (b) Detection characteristics of the MI sensor .

2.2.4 Noise Level of the MI Sensor

Figure 2.6 illustrates the noise spectral density of the MI sensor, with or without a magnetic shielding room, as a reference. After 60 seconds measurement and the amplification (A=1000), the signals were filtered by a 60 Hz notch filter to remove the commercial power source noise. In order to evaluated the performance of the sensor circuits, the digital processing functions of the system were all turned off except the basic functions as a data logger. The noise level is lower than 2 mv (about 6 pT) without the shielding room and lower than 1 mv (about 3 pT) inside the shielding room.

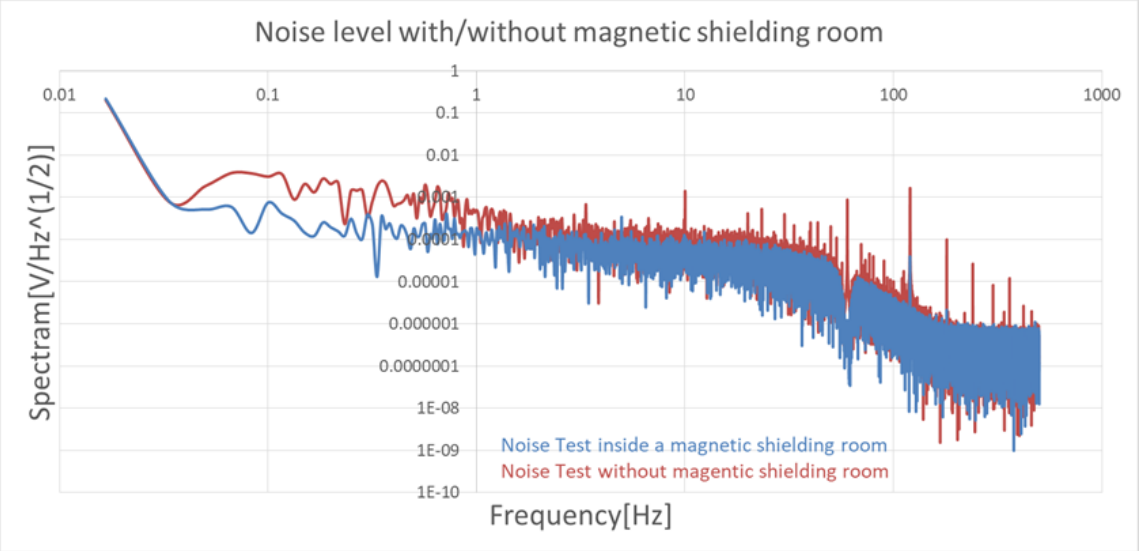

Figure 2.6 The noise spectral density of the MI sensor. Red: Noise test without magnetic shielding room. Blue: Noise test with a magnetic shielding room.

Chapter 3

Measurement of Single-channel Off-line System

3.1 Single-channel Off-line System

In this part, the goal is to review the performance of MI sensor by measuring the N100 AEF and P300 ERF brain activites using the single-channel off-line system. Figure 3.1 shows the schematic diagram of the system. The entire sensor circuits, include sensor head, were fixed on a four-joint support arm, which could be rotated in 360 degrees. After amplified for 1000 times, a 60 Hz notch filter was used to remove the commercial power source noise, and a 45 Hz low-pass filter was used to remove the high frequency noise components. Both of those two filters were analog. The signals were sampled with 1000 Hz rate and recorded by a data logger, which has a 14 bit AD converter. A microcontroller was programed to generate the auditory stimuli using C language. All off-line signal processing was programmed by Matlab. Figure 3.2 shows the basic functions of the single-channel off-line processing system. The digital filter was designed based on Fast Fourier transform (FFT) and Inverse FFT (IFFT), which had a frequency bandwidth from 0.5-30 Hz.

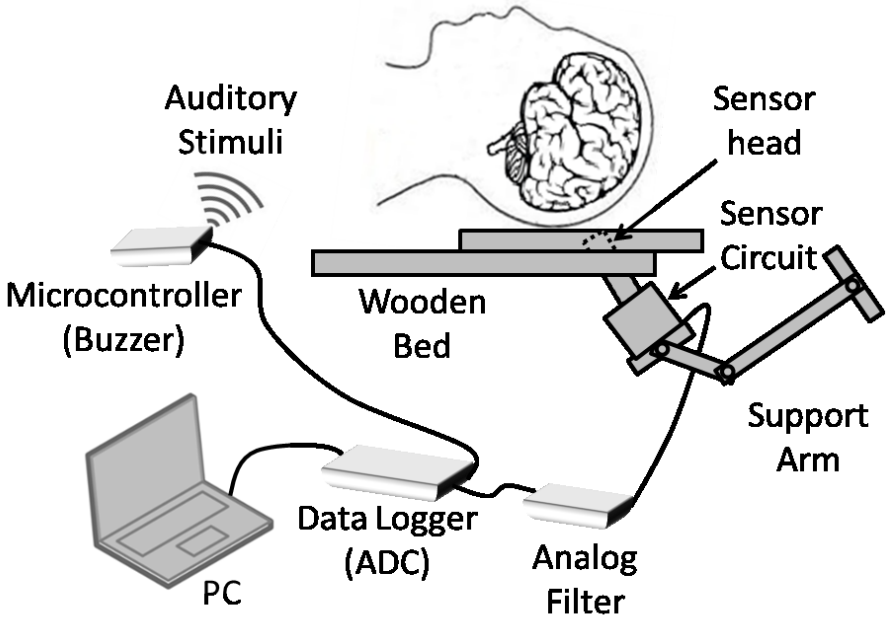

Figure 3.1 The schematic diagram of the single-channel off-line processing system.

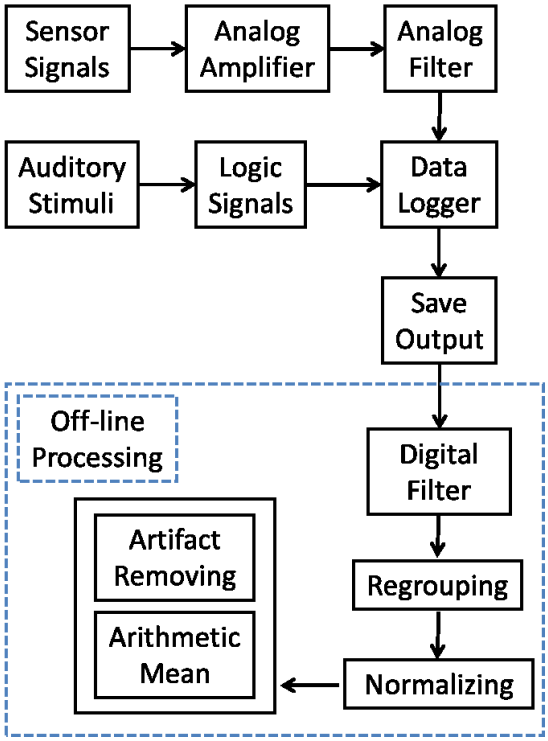

Figure 3.2 Basic functions of the digital signal processing for single-channel off-line processing system.

3.2 N100 AEF Measurement

Two single-channel MI sensors were used in this measurement (the signals of those two sensors were record at the same time but they were processed independently without using any multivariate statistics. So in this study I perfer “two single-channel” rather than “two-channel”). As introduced in 1.7.2, the auditory N100 is induced by auditory stimuli, so in this study we used the buzzer of a microcontroller to generate the auditory stimuli (1000 Hz).

3.2.1 Configuration & Methods

The subject (24-year-old female with normal auditory perception and no neurological or psychiatric problems reported) laid comfortably on a wooden bed with a relaxed state of mind. Two MI sensors were set contactlessly on the left temporal (T3) and the right temporal (T4) region of the International 10-20 system, as shown in figure 3.3. The distance between the MI sensor head and the scalp of subject was 5 mm. The subject kept her eyes open (blinking was acceptable) and heard the auditory stimuli. The duration of one stimulus was 200 ms. Interval time between two stimuli was random, from 800 ms to 1200 ms. A total of 500 auditory stimuli were presented on the subject. The subject could take a break for 30 second every 50 stimuli, but could not leave the wooden bed to prevent the slide of measurement positions. The microcontroller (sound source) was set on the left side of the subject with a 1 m distance. After recording, 500 stimuli conditions were

obtained and 100 of them with no artifacts were chosen for arithmetic averaging.

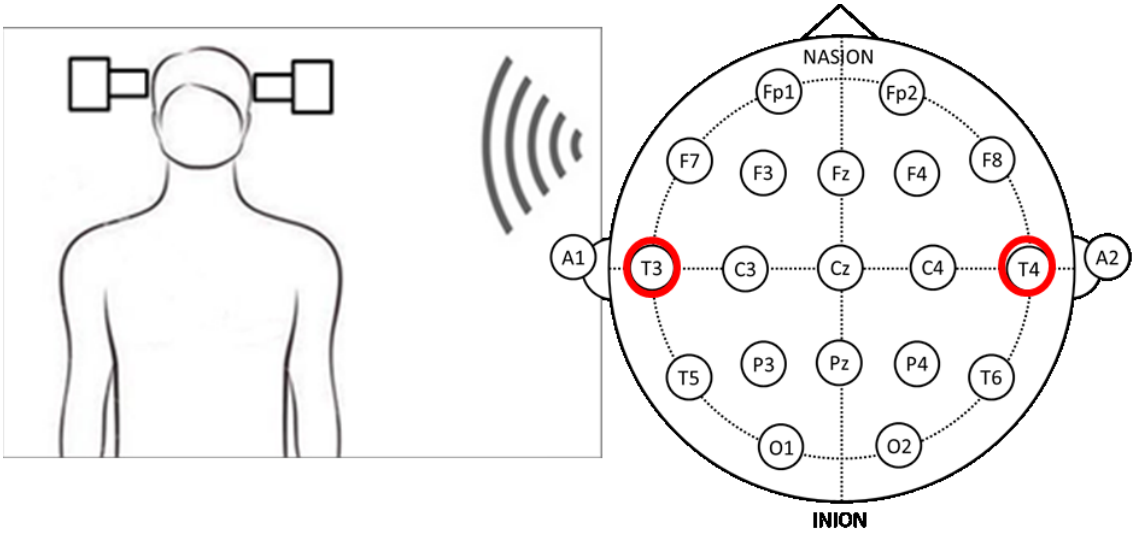

Figure 3.3 MI sensor was set contactlessly on the left temporal (T3) and the right temporal (T4) region of the International 10-20 system.

3.2.2 Results & Discussion

The measurement was repeated 3 times (task 1, 2, 3) and the brain activity waveforms are displayed in figure 3.4. All of them were processed in the same fashion. The results show that deflections with a latency of approximately 115 ms can be elicited by the auditory stimuli, and the polarity of deflections on the left and right temporal regions is opposite. It is positive on the right temporal (T4) and negative on the left temporal (T3) region. All 3 tasks present common characteristics. compared our results with other results of the N100 research[27, 28, 49], which reported the

measurement of brain activity by EEG and MEG. Figure 3.5 shows the comparison of N100 AEF from [49, fig 1] and our results. The waveforms show similar characteristics with our results.

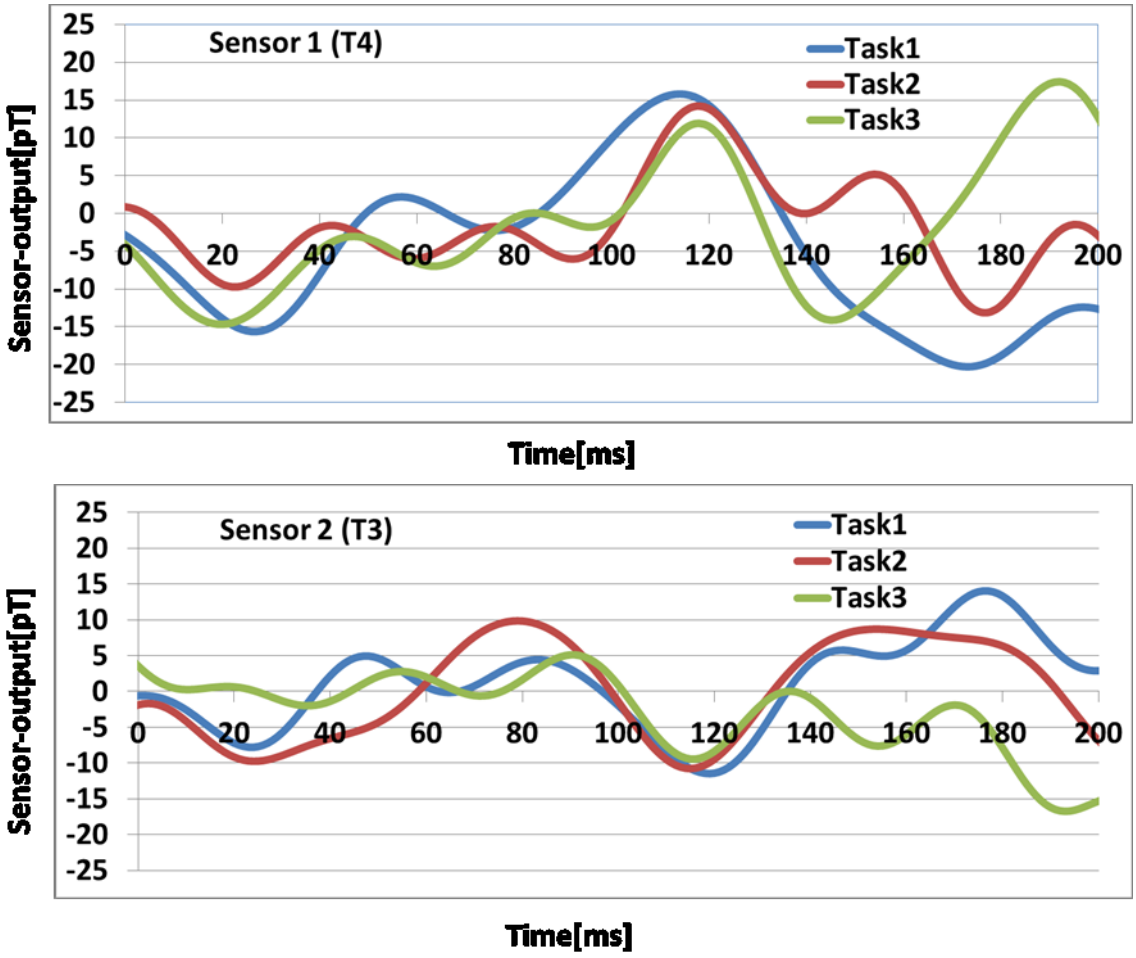

Figure 3.4 The averaged N100 AEF brain activity waveforms measured on the left temporal (T3) and the right temporal (T4) region.

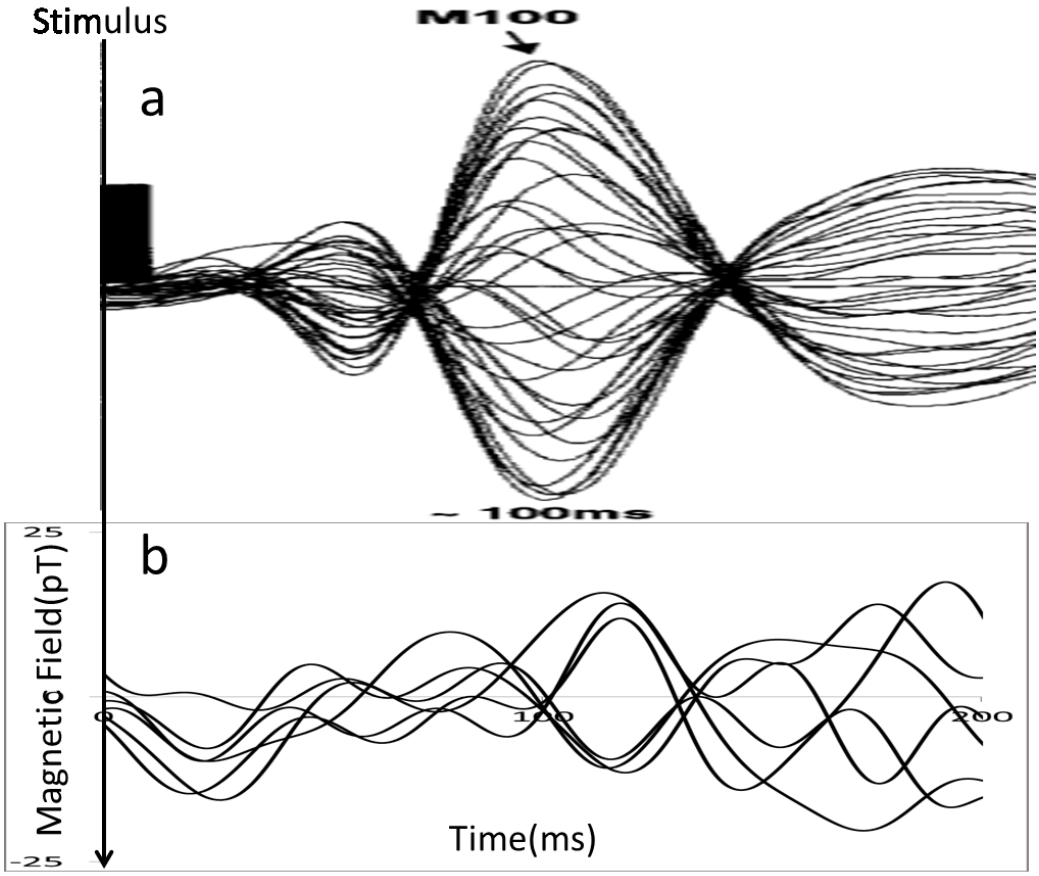

Figure 3.5 The comparison of N100 AEF from [49, fig 1] and the results measured by MI sensor. (a) An auditory evoked neuromagnetic field as recorded by MEG (37-channel, waveforms of 0-200 ms). (b) waveforms of brain activity induced by auditory stimuli measured by MI sensor on the left (T3) and the right (T4) temporal regions (figure 3.4 plots in one figure).

In this study, I measured N100AEF using two single-channel off-line system on the left (T3) and the right (T4) temporal regions. At the very beginning of designing the system for N100 AEF measurement, the duration of one stimulus was 200 ms but interval time between two stimuli was a

constant (800 ms). The results of N100 AEF were not obvious. Based on other N100 research[29], the N100 shows a link to a person's selective attention. It seems that the fixed interval time between two stimuli makes the stimuli divinable and the N100 is easy to disappear when a person could predict the next auditory stimuli. So I changed the interval time to random to reduce this influence. Also as the sensor head and the scalp of the subject was contactless, for MEG measurement, the direction and amplitude of the magnetic field could be different by a slight movement [44, figure 1]. Even though the subject would not leave the wooden bed during the rest but it was still very difficult to keep the measurement postition. For example, as the distance between the sensor head and scalp of the subject was only 5 mm, the sensor head was easily touched by the hair or ears, and it will change the measurement position sometime. It also happened in P300 ERF measurement.

3.3 P300 ERF Measurement (Induced by Auditory Stimuli)

The most common task used to induce the P300 ERP/ERF is called "Oddball paradigm" as shown in figure 3.6. It is a selective attention task that usually consist of two series of events, target and standard stimuli (two-stimuli odd-ball paradigm). During the task, subjects are instructed to respond and to ignore the target and standard stimulus, respectively[30]. The sensor system records the brain activity of the subjects and analyze

what is different when subjects face those two kind of stimuli. There are many types of stimuli used in the oddball paradigm, such as olfactory, taste and somatosensory stimuli. But comparing with the auditory and visual stimuli, they are less used in clinical application because they could be easily affected by individual difference and the starting of stimulation is difficult to confirm. In this study, the brain activity was measured by a single-channel MI sensor and the P300 ERF was induced by auditory stimuli using the microcontroller.

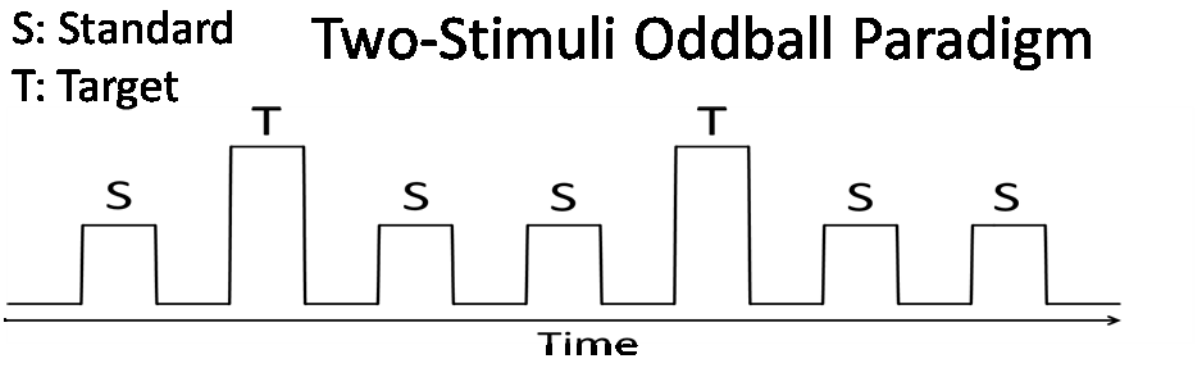

Figure 3.6 Two stimuli oddball paradigm used to induce the P300 ERF.

3.3.1 Configuration & Methods

There are 3 subjects (2 males and 1 female between the ages of 21- 28 with normal auditory perception and no neurological or psychiatric problems reported) were asked to do the two-stimuli oddball paradigm in this study. Subject lay comfortably on a wooden bed with relaxation of mind and put his/her index finger on a response button. The MI sensor was set

contactlessly on the parietal (Pz) region of the International 10-20 system, as shown in figure 3.7. The distance between sensor head and the scalp was 5 mm. Two kinds of auditory stimuli, low probability (p = 0.2) target stimuli (2000 Hz), and high probability (p = 0.8) standard stimuli (1000 Hz), were presented in a random series once every 1500 ms in the P300 ERF measurement. A total of 300 stimuli were presented to the subject (target stimuli = 60, standard stimuli = 240). The subjects were asked to keep their eyes open (blinking was acceptable) and heard the auditory stimuli. The duration of one stimulus was 50 ms. Interval time between two stimuli was 1450 ms. As with the N100 AEF measurement, The subject could take a break for 30 second every 30 stimuli, but could not leave the wooden bed. After recording, 60 target stimuli conditions and 240 standard stimuli conditions were obtained from each subject and 30 conditions with no artifacts were chosen for arithmetic averaging, respectively.

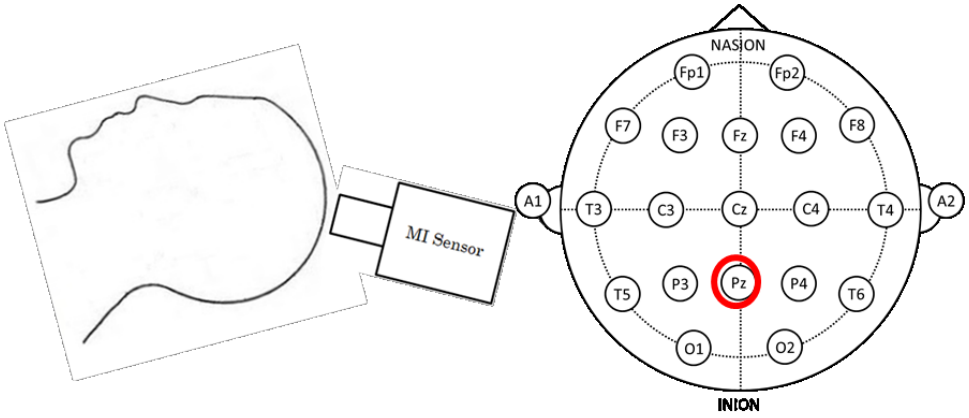

Figure 3.7 The MI sensor was set contactlessly on the parietal (Pz) region of the International 10-20 system.

3.3.2 Results & Discussion

The brain activity waveforms from three subjects are displayed in figure 3.8. From top to bottom, it shows the rusult of male A (26-year-old), female B (21-year-old) and male C (29-year-old). The red and blue line are the averaged brain activity when target and standard stimuli presented. Both target and standard conditions were processed in the same fashion. The results show that the positive deflections with a latency of approximately 300-400 ms can be elicited by target stimuli appreciably but barely elicited by standard stimuli, and the 3 graphs presented common characteristics. However, male A and female B shows more common characteristics than that of male C and the result of male C has the higher amplitude and shorter latency.

In P300 ERP measurement, three subjects performed the two-stimulus oddball task and the results show similar characteristics. Figure 3.9 (a) and (b), which we reported in the previous work[50], show the waveforms of mean P300 ERP elicited by target and standard stimuli in occipital (Oz, between O1 and O2) region and waveforms of 3 times repeated measurement of the same subject (the male C reported in figure 3.8). The waveforms clearly possess similar characteristics with the waveforms shown in figure 3.8. However, it seems that the latency of the male C's brain activities is usually around 300 ms and shorter than the male A and the female B. We also compared our data with other P300 ERP relevant research results[40,51], which detected the brain activity by EEG electrodes and

arrays of SQUIDs, the waveforms show the similar characteristics with our data, even though there is a minute difference in amplitude and latency due to different objective and subject situation.

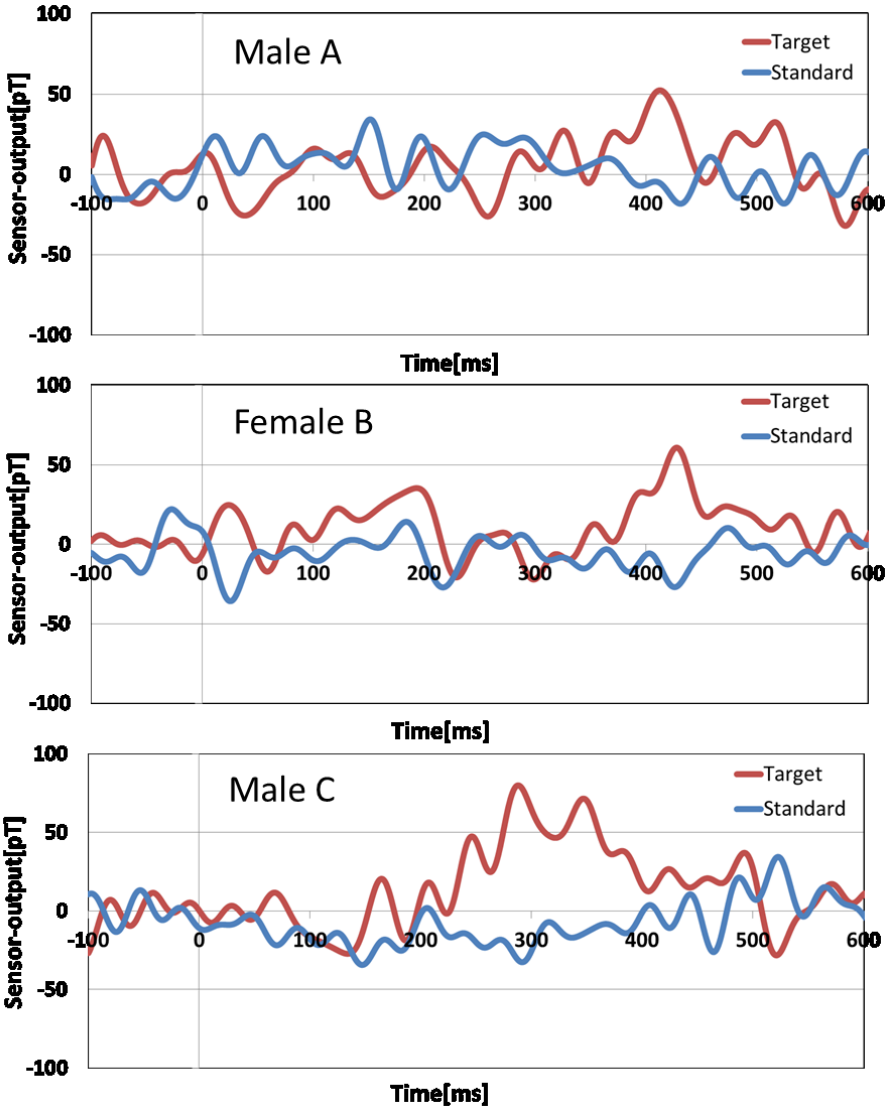

Figure 3.8 The averaged P300 ERF brain activity waveforms from 3 subjects measured on their parietal (Pz) region. The red and blue line are the averaged brain activity when target and standard stimuli presented.

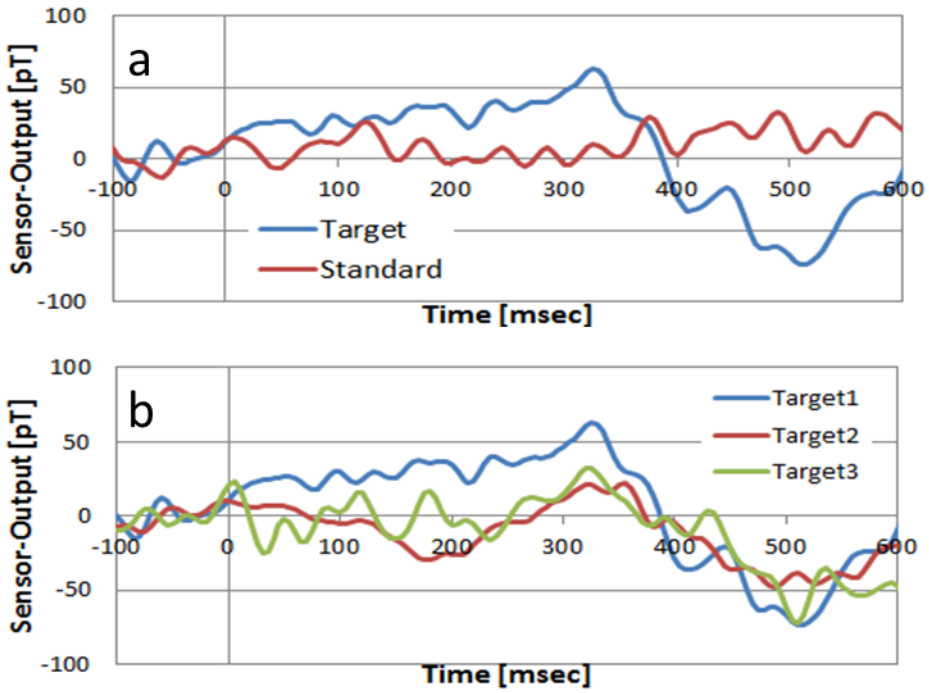

Figure 3.9 The waveforms of ERP we reported in past work. (a) shows the waveforms of mean P300 ERP elicited by target and standard stimuli in occipital region. (b) shows the waveforms of 3 times repeated measurement of the same subject (male C)[50].

Chapter 4

Measurement of Single-channel Real-time System

4.1 Single-channel Real-time System

In this part, I aimed to improve the single-channel off-line system for a better performance and could be used in more applications in the future, such as BCI. I first improved the signal processing module to process the signals faster and in real-time, then the stimuli generator (both auditory and visual) was developed and integrated into the single-channel real-time system, which the parameter could be adjusted during different tasks. I also changed a high-precision 24-bit AD converter for higher resolution. In this part, I measured the alpha rhythm and the P300 ERF brain activites using the single-channel real-time system. Figure 4.1 shows the schematic diagram of the improved single-channel real-time system. The sensor head was fixed into a polystyrene box, which could be set anywhere on the scalp.

The visual/ auditory stimuli generator and real-time signal processing was designed by LabVIEW, Matlab FDA tool and microsoft visual studio (c/c++), off-line signal processing was programmed by Matlab. Figure 4.2 shows the basic functions of the digital signal processing module for real-time

processing system. Depending on the theme of the task, visual or auditory stimuli were created by the stimuli generator and presented to the subject. The sensor detected those brain activites, then signals were sampled every millisecond (fs=1000 Hz) and recorded by a 24 bit AD converter (± 10 V, 1 μV resolution). The main digital filter was designed as a 24-order Chebyshev II type IIR filter, which has no ripple in the passband. As the brain activities I interested were in a frequency bandwidth from 1 to 30 Hz, the passband of the main filter was set in a frequency bandwidth from 0.1-40 Hz and the stopband attenuation is 60 dB. Then according to the different characteristics of those brain activities, the signals will be pre-processed differently. For example, when measuring P300 ERF, the passband of the sub-filter will be set in a frequency bandwidth from 1-9 Hz to reduce the high frequency components, and the signals need to be regrouped to standard and target serie to run a arithmetic mean individually. Beside the real-time processing, the data can be saved and outputed to run a off-line processing such as multivariate analysis or time-frequency analysis.

Also figure 4.3 illustrates the noise spectral density of the single-channel real-time processing system, which the frequency bandwidth of the main digital filter was set on 0.1-40 Hz without the magnetic shielding room, the noise level is about 4 pT.

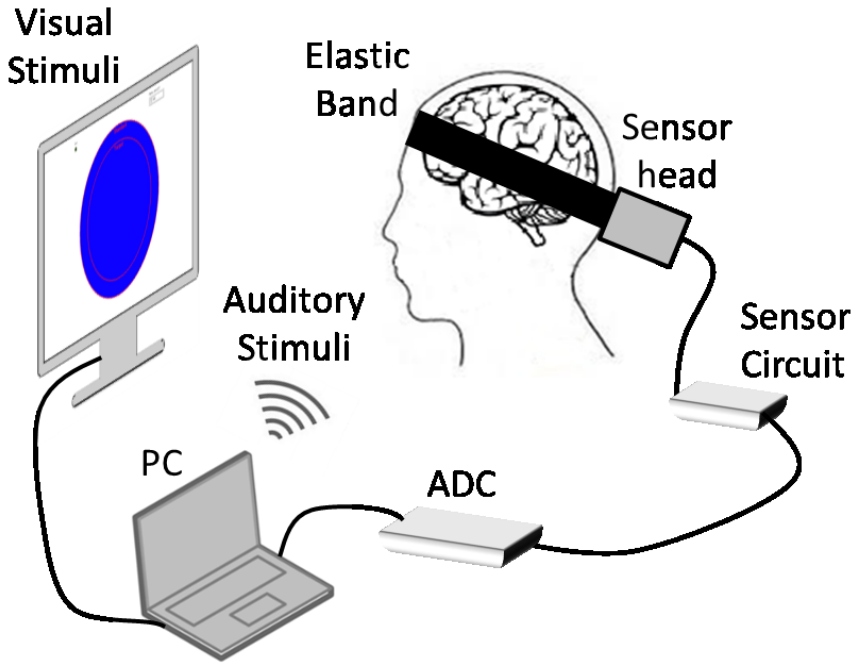

Figure 4.1 The schematic diagram of the single-channel real-time processing system.

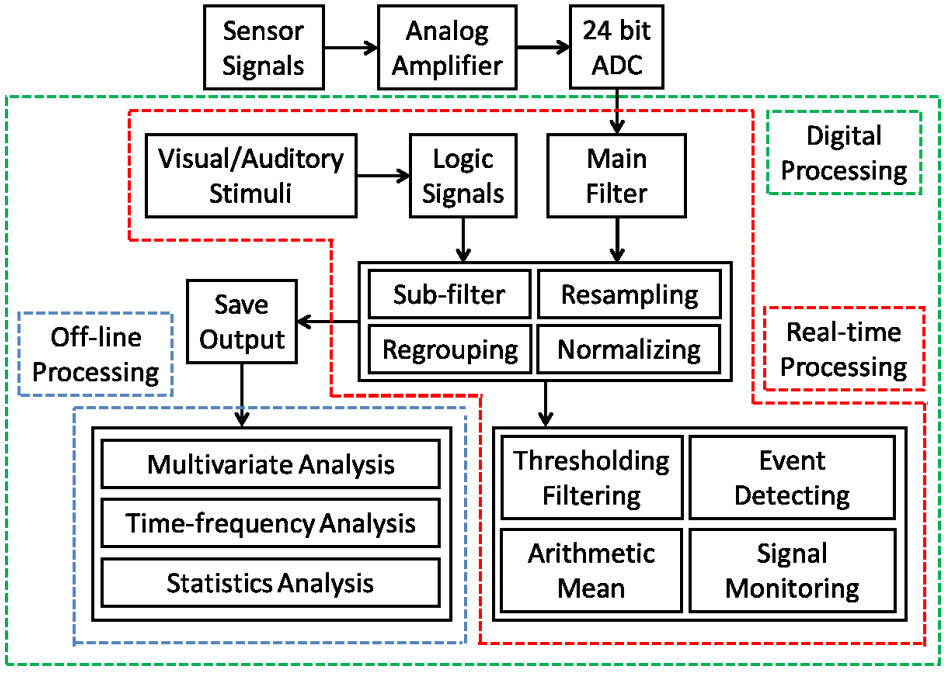

Figure 4.2 Basic functions of the digital signal processing module for real-time processing system.

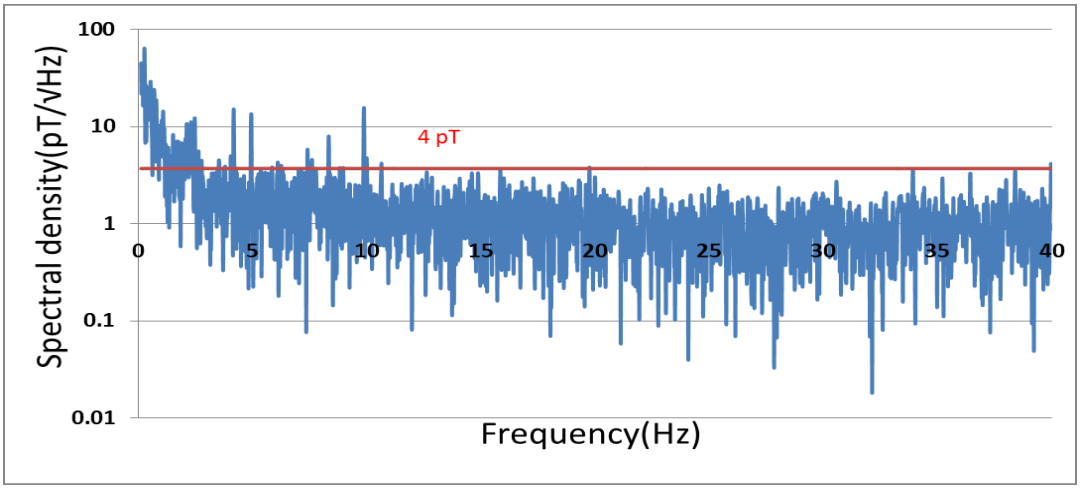

Figure 4.3 The noise spectral density of single-channel real-time processing system with 0.1-40 Hz digital BPF

4.2 Alpha Rhythm Measurement

As one of the neural oscillations, the alpha rhythm, with a 8-13 Hz frequency range, can be easily identified at a maximum amplitude over the occipital region. Due to the large amplitude of the alpha rhythm, it can be an influential factor during other brain activity measurements, such as P300 ERF. Furthermore, the alpha rhythm usually appears in relaxed wakefulness with eyes closed, drowsiness period and REM sleep stage, and the amplitude attenuate with the eyes opening[31]. During information processing, lots of the neurons in the brain show less synchronous oscillation than those in a resting state and it results in localized and transient blocking of EEG alpha rhythm. This amplitude attenuation or blocking of the alpha rhythm is related to an internally or externally paced event, termed event-related desynchronization (ERD)[32]. The ERD occurs in a specific frequency band in a brain region relating with a task or information

given[33]. Eye opening task with input of visual information causes alpha ERD in the occipital area in most human subjects. Also the ERD is not only found with EEG but also with MEG recordings[34].

4.2.1 Configuration & Methods

As the alpha rhythm has different amplitude when subject close or open his eyes, in this study, I designed the processing module that measures and records the brain signals for frequency analysis confirm the change.

The subject (a 29-year-old healthy male with no neurological or psychiatric problems reported) sat in a comfy wooden chair (no metals inside) with a relaxed state of mind. His neck was supported to reduce the movement artifacts caused by the fatigue during whole measurement. The sensor head was set on the middle of the occipital region (position between O1 and O2 of the International 10-20 system), as shown in figure 4.4 (a). As the thickness of the polystyrene box was 5 mm, so the distance between MI sensor head and scalp of the subject was considered as 5 mm. During the measurement, the subject was instructed to open or close his eyes every 30 seconds with a beep, as shown in figure 4.4 (b). In order to extract the alpha rhythm component, a 7-14 Hz bandpass filter was applied, then the brain signals of both eyes closed and open situation, was processed for spectral analysis to observe the variations in the frequency area.

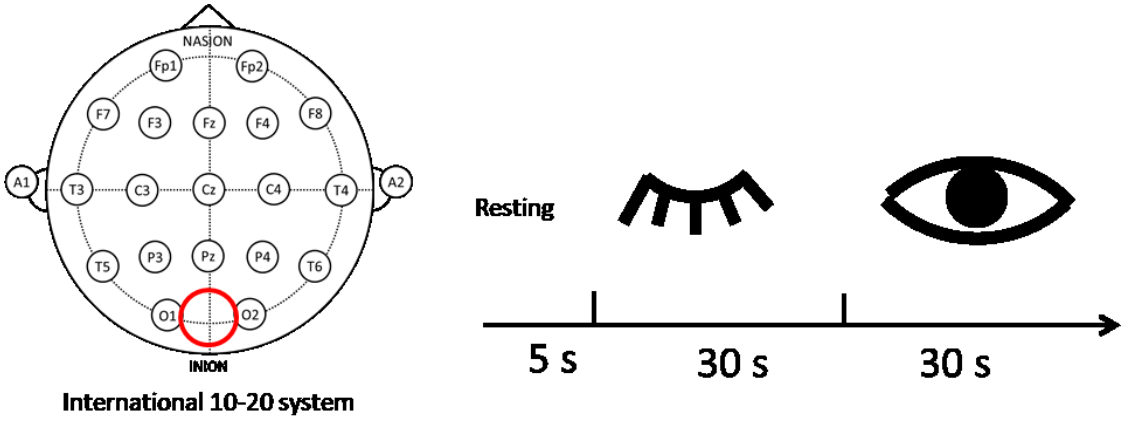

Figure 4.4 (a) MI sensor was set on the position between O1 and O2 of the International 10-20 system.(b)The subject closed and opened his eyes repeatedly every 30 seconds

4.2.2 Results & Discussion

Figure 4.5 shows a part of the filtered sensor signals (3 seconds) in both eyes closed and open situations. Figure 4.6 (a) and (b) show the spectral density and the sum power spectrum level of all 60 seconds measurement (30 seconds with eyes open and 30 seconds with eyes closed). The results show that when the subject opened his eyes, not only the signal amplitude was attenuated, but also the sum power spectrum in every Hz level of the 8-13 Hz frequency band was observably attenuated than eyes closed situation, especially in 10 Hz.

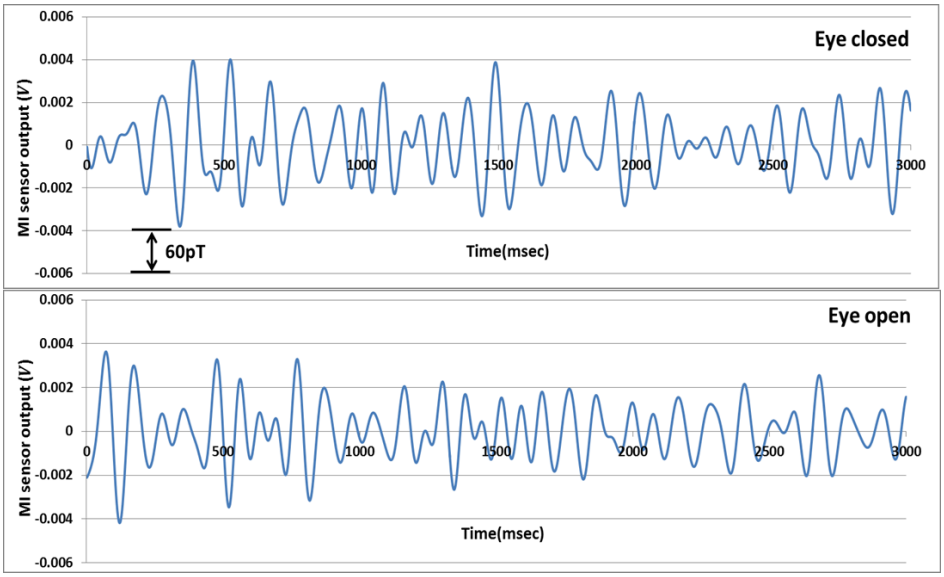

Figure 4.5 Waveforms(3 s) of brain activity when subject closed / opened his eyes

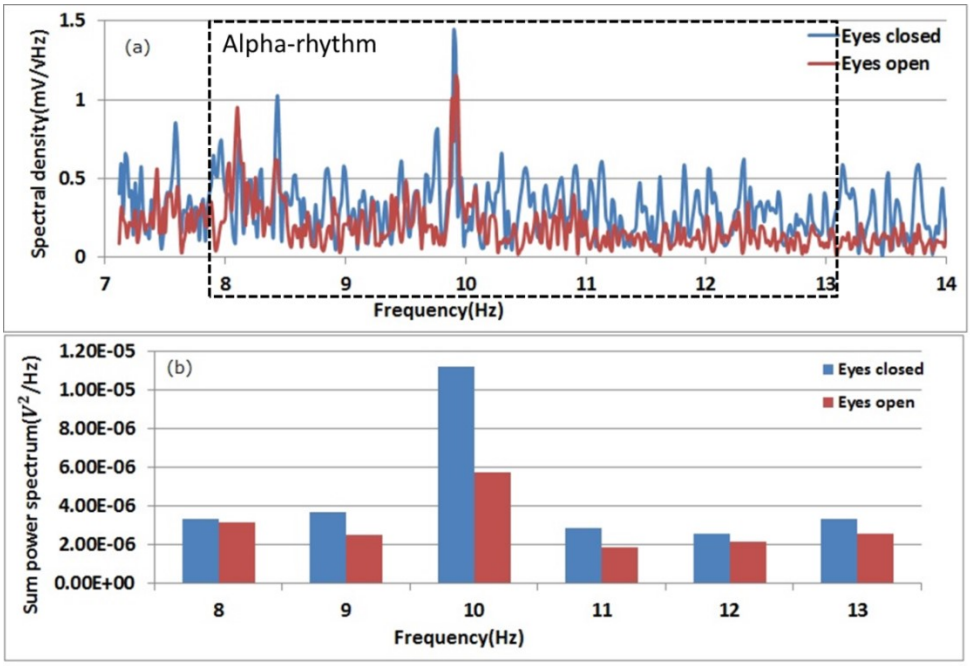

Figure 4.6 Spectral density and the sum power spectrum of 60s measurement.

I also run an off-line time-frequency analysis to calculate the difference between closed and open conditions (PS_{closed}-PS_{open}), and the result is shown in figure 4.7. It shows the trend that comparing with the 7-14 Hz brain activity with eyes opened, the activity is stronger when eyes closed. Also it shows a periodic fluctuation that increases and decreases every several seconds in 10 Hz.

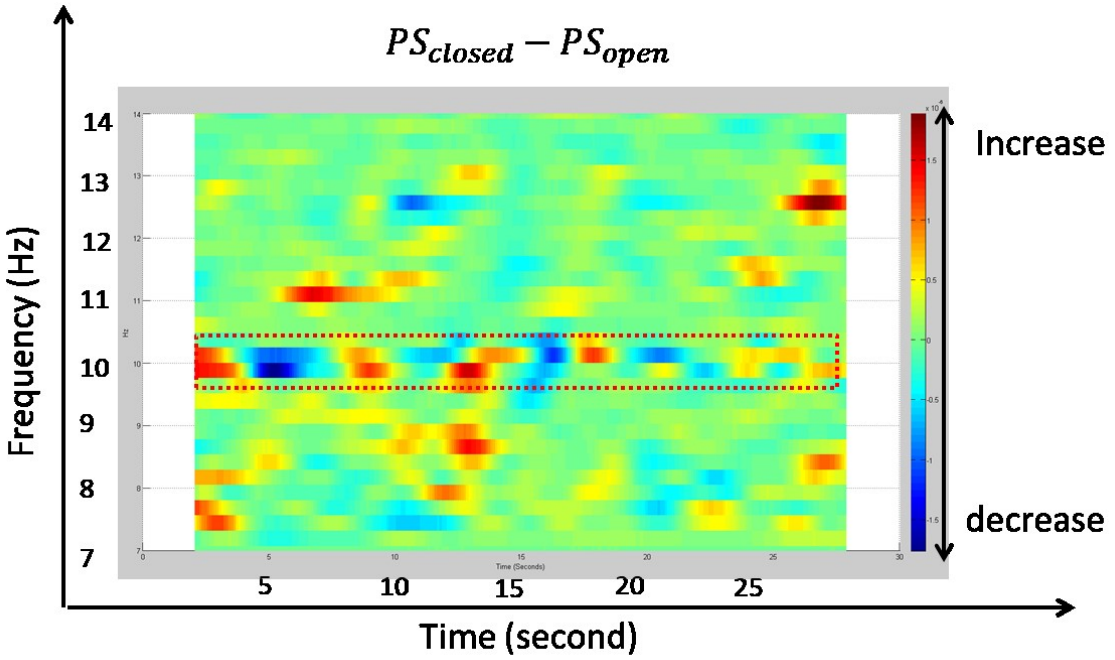

Figure 4.7 Time-frequency analysis of the 7-14 Hz brain activity signal.

Depending on the reference [35-37], it seems that the periodic fluctuation is caused by a feature of alpha rhythm called " waxing and waning". It means that the the amplitude of the alpha rhythm is not constant, it will occurs for a period of several seconds with a change of the amplitude.

I referred the experiment methods and compared our results with other

alpha rhythm research by EEG and MEG [38,39, 52], it was confirmed that when the subject opened his eyes, the intensity of the alpha rhythm was considerably reduced and the main spectral contribution was observed in the 10 Hz frequency component. A comparison of the alpha rhythm from [52, fig 2, A and B] and our results is shows in figure 4.8.

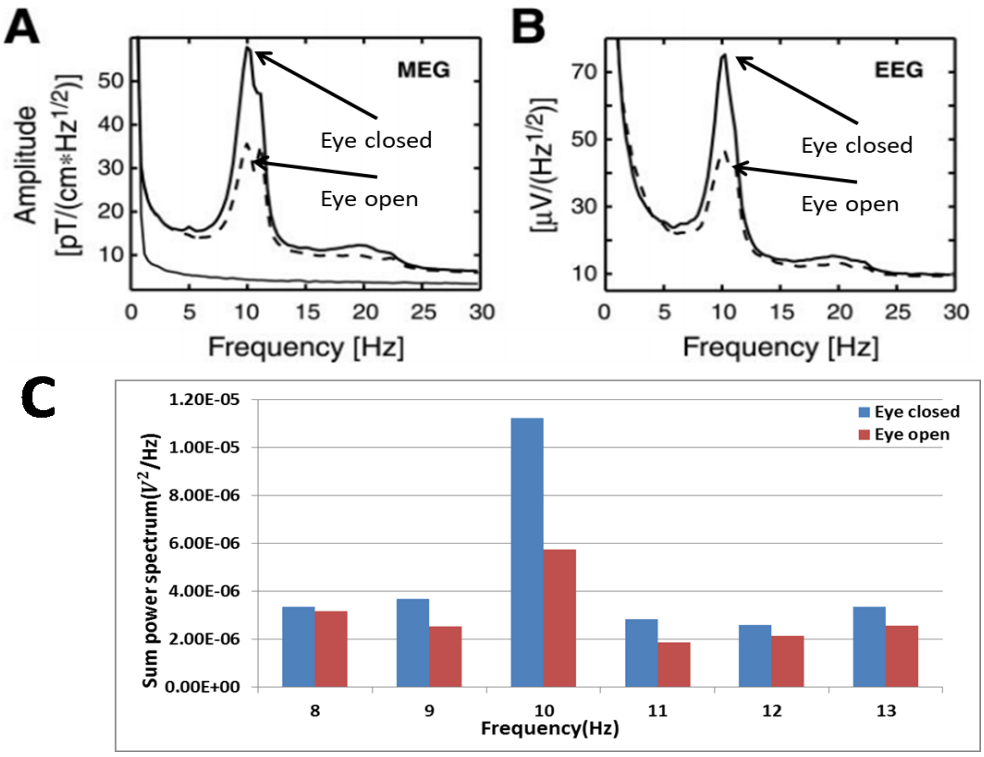

Figure 4.8 Grand average (n = 10) amplitude spectra of conditions eyes-closed (thick solid line) and eyes-open (thick dashed line) display large peaks in the alpha frequency band in the occipito-parietal region of MEG (A) and EEG (B)[52]. (C) is the sum power spectrum measured by MI sensor. It it obviously that when the subject opened his eyes, the alpha rhythm was considerably reduced and the main spectral contribution was observed in the 10 Hz frequency component.

4.3 P300 ERF Measurement (Induced by Visual Stimuli)

As with the auditroy stimuli induced P300 ERF reported in 3.3, in this part, the brain activity was measured by a single-channel MI sensor and the P300 ERF was induced by visual stimuli this time. As said in 3.3, different types of visual stimuli, such as photos, characters and different shapes are used in visual oddball paradigm. Actually, the very first version of the visual stimuli was two circles with different color. But soon I realized that it is harder to balance the difficulty between two colors than two sizes, because I neither want the task be too hard nor too easy. At last I decided to use two different sizes of shape as visual stimuli, but the others are optional too. Figure 4.8 shows examples of visual stimuli produced by the system, the paramater, such as radius ratio, shape or color of standard and target stimuli, could be adjusted in different tasks.

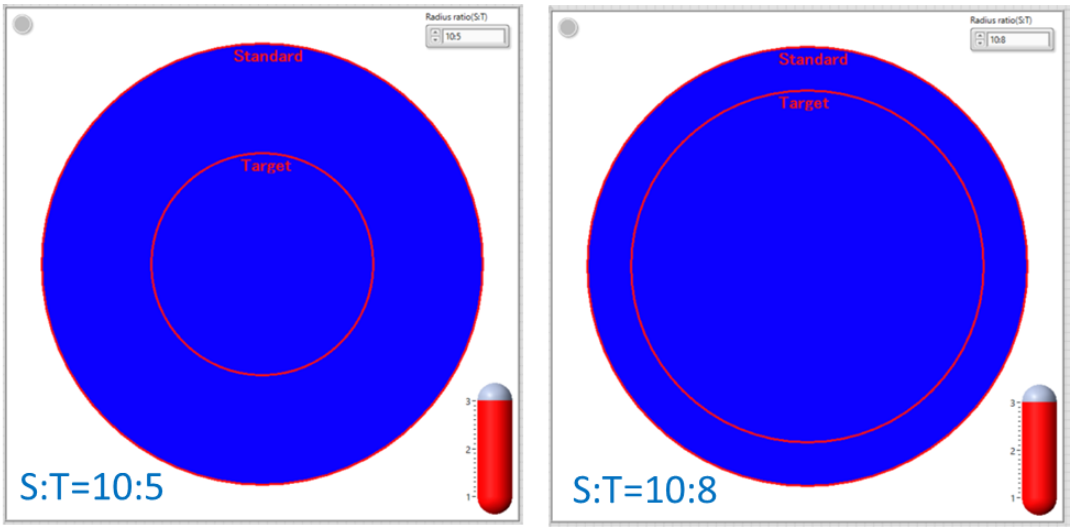

Figure 4.8 Visual stimuli produced by the system. The radius ratio of standard and target stimuli is 10:5 (left) and 10:8 (right).

4.3.1 Configuration & Methods

On visual stimuli induced P300 ERF measurement, one subject (a 29-year-old healthy male with no neurological or psychiatric problems reported) was asked to do the two-stimuli oddball paradigm 4 times. In this task, two kinds of visual stimuli were frequently presented on a screen in front of the subject in a random series once every 800 ms (400ms duration and 400 ms interval time). The standard stimulus had a large radius (r=10) and a high probability (p=0.8), and the target stimulus had a small radius (r=8) and a low probability (p=0.2), as shown in figure 4.8 (right). When a target stimulus was presented, the subject was instructed to press a response button to indicate it as quickly as possible, but no indication for a standard stimulus.

In order to see the distribution of P300 ERF, the sensor head was set each on the frontal (Fz), parietal (Pz), left temporal (T3) and right temporal (T4) region of the scalp respectively in those 4 experiments as shown in figure 4.10. Moreover, the subject was fully awake and asked to keep his eyes open (blinking was accepted) to reduce the influence caused by alpha rhythm. Different from alpha rhythm, on P300 data processing, after applying a bandpass filter in 1-9 Hz frequency band, a range filter was applied to remove the data with over range, which was normally caused by subject movement. Then the data were divided into the standard and the target conditions, and 100 standard and target conditions were chosen for arithmetic averaging in the same method respectively. Flowchart of the real-time P300 ERF signal processing module was shown in figure 4.9.

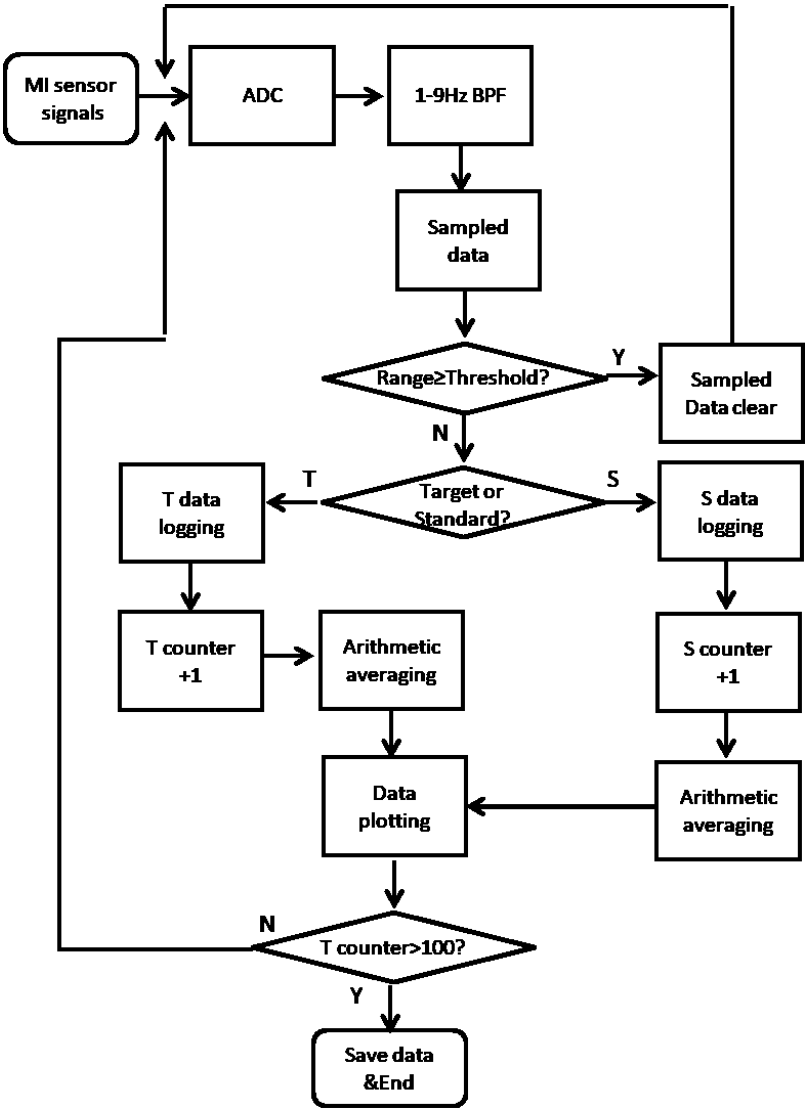

Figure 4.9 Flowchart of the real-time P300 ERF signal processing module.

4.3.2 Results & Discussion

The averaged P300 brain activity waveforms measured in four regions (Fz, Pz, T3 and T4) are displayed in figure 4.10. The results show that in parietal and the right temporal region, positive deflections with a latency of 300 ms can be observably elicited by target stimuli, but barely elicited by standard

stimuli, but in frontal and left temporal region, the deflections are negative, and the latency times are 300-400 ms.

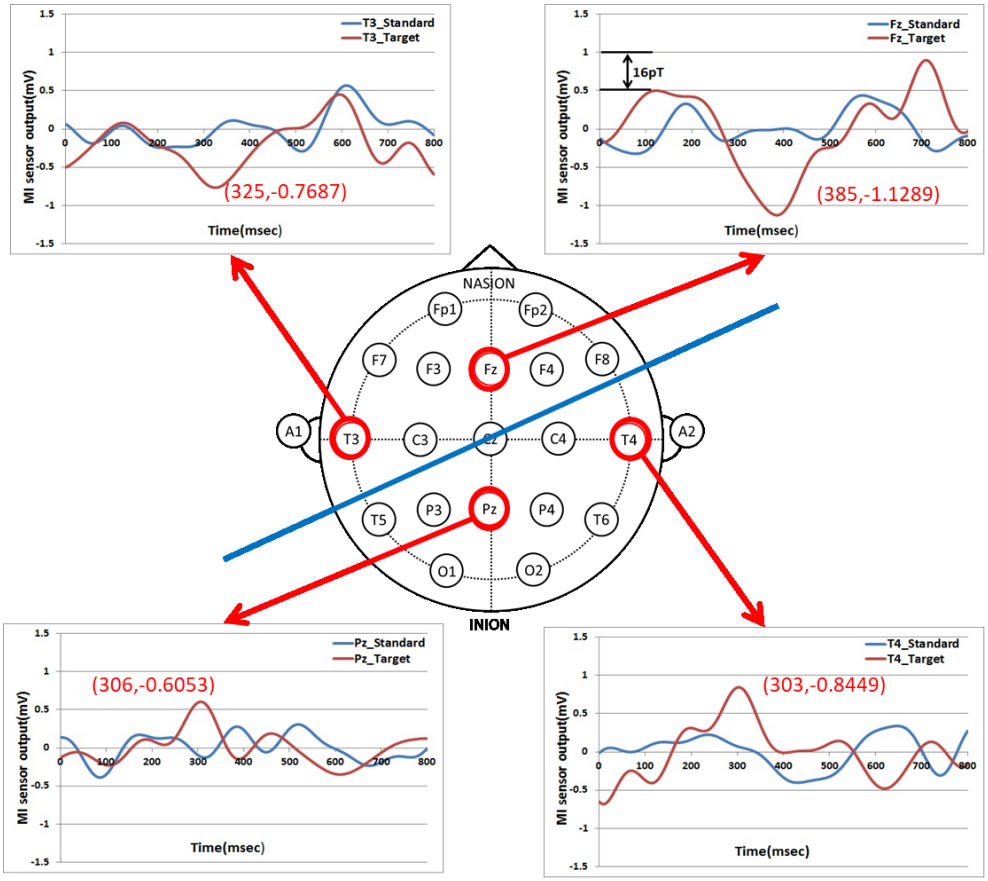

Figure 4.10 The averaged P300 brain activity waveforms measured in the frontal, the parietal and both the temporal regions.

On P300 measurement, I referred to other results of MEG research based on visual stimuli elicited P300[40], and our past study[17,18], the deflections can be elicited by the target but not by the standard stimuli around 300-400 ms and the results showed similar characteristics to our results in this study. Furthermore, the absolute value of a P300 peak was measured in about 19.97-37.23 pT (1 mV is about 30 pT). Figure 4.11 shows the sketch of the

measurement model.

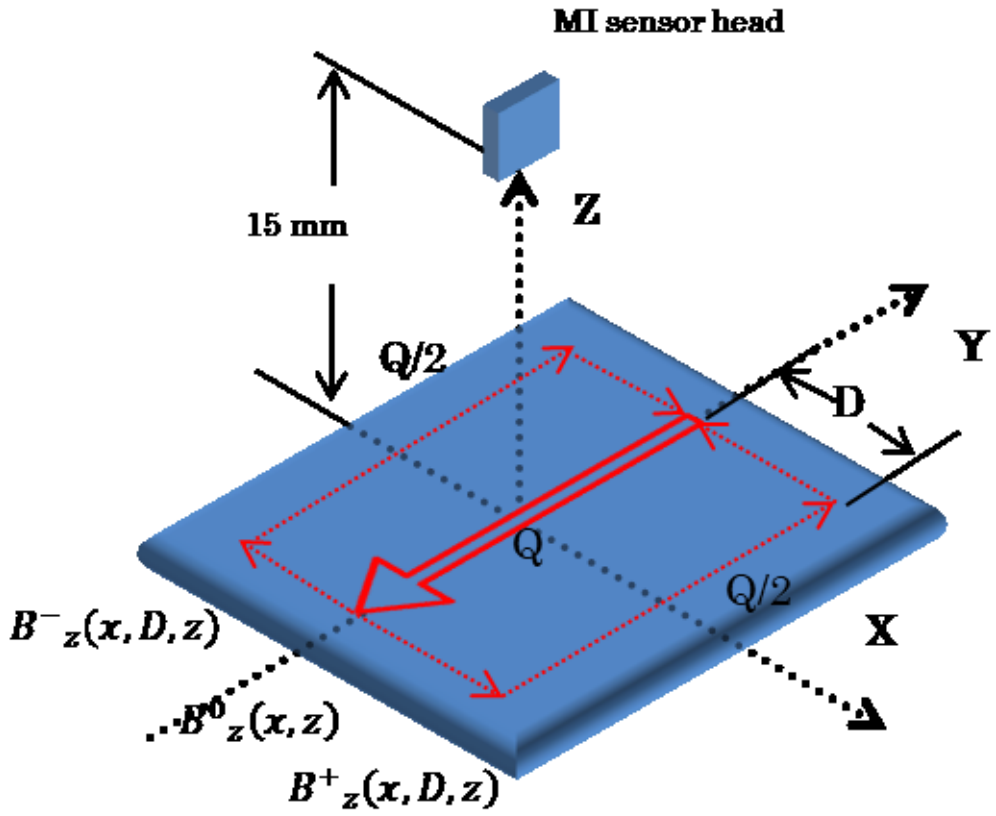

Figure 4.11 The sketch of the measurement model used in this study.

In this model, the brain surface is locally treated as a plane. The **r** is the position of the sensor, $\mathbf{r}_Q$ is the position of the current dipole. The **Q** is the brain current dipole source, e_z is the unit vector normal to the surface, the red arrows represent the current direction (dash line is return current). Assuming the distance between current dipole source and the return current is D. The distance between the cerebral cortex and the MI sensor head is z.

The Z direction magnetic field (Bz) generated by a current dipole located within a horizontally layered conductor is given by [41, equation 35]

$$B_z = \frac{\mu_0}{4\pi}\frac{\boldsymbol{Q}\times(\boldsymbol{r}-\boldsymbol{r_Q})\boldsymbol{e_Z}}{|\boldsymbol{r}-\boldsymbol{r_Q}|^3} \tag{4.1}$$

The Bz along x axis are as follows:

$$B_z(x,D,z) = B^0{}_Z(x,z) + B^+{}_Z(x,D,z) + B^-{}_Z(x,D,z) \tag{4.2}$$

$$B^0{}_Z(x,z) = \frac{\mu_0 Q}{4\pi}\frac{x}{\sqrt{(x^2+z^2)^3}} \tag{4.3}$$

$$B^+{}_Z(x,D,z) = \frac{\mu_0}{4\pi}\frac{Q}{2}\frac{D-x}{\sqrt{((D-x)^2+z^2)^3}} \tag{4.4}$$

$$B^-{}_Z(x,D,z) = \frac{\mu_0}{4\pi}\frac{Q}{2}\frac{x}{\sqrt{((D+x)^2+z^2)^3}} \tag{4.5}$$

where μ_0 is the vacuum permeability. Using this model on SQUIDs, the z is about 60 mm, assuming the Q is 100 nAm [42], D is 20 mm, and the maximum value of magnetic field is estimated as 0.18 pT when x is 10.8 mm (experimental value is about 0.2 pT [23, Fig.3]). Then using the same model on MI sensor, z is about 15 mm (the distance between cerebral cortex and scalp is roughly 10 mm). the maximum value of magnetic field Bz is estimated as 21.71 pT and it is about 120 times bigger than the estimated value of SQUIDs.

In addation, I run an integration of EEG electrodes/MI sensor to measure the P300 ERP/ERF cooperated with other group. In this task, EEG electrods were set on position Fz, Cz, Pz, O1 and O2, also reference potential was record by electrods set on the left (A1) and right (A2) earlobes. MI sensor was set on position T4 (shown in figure 4.12 (a)). In this task, there were 4 pairs

of visual standard/target stimuli with different radius ratio presented on the display, as shown in figure 4.12 (b).

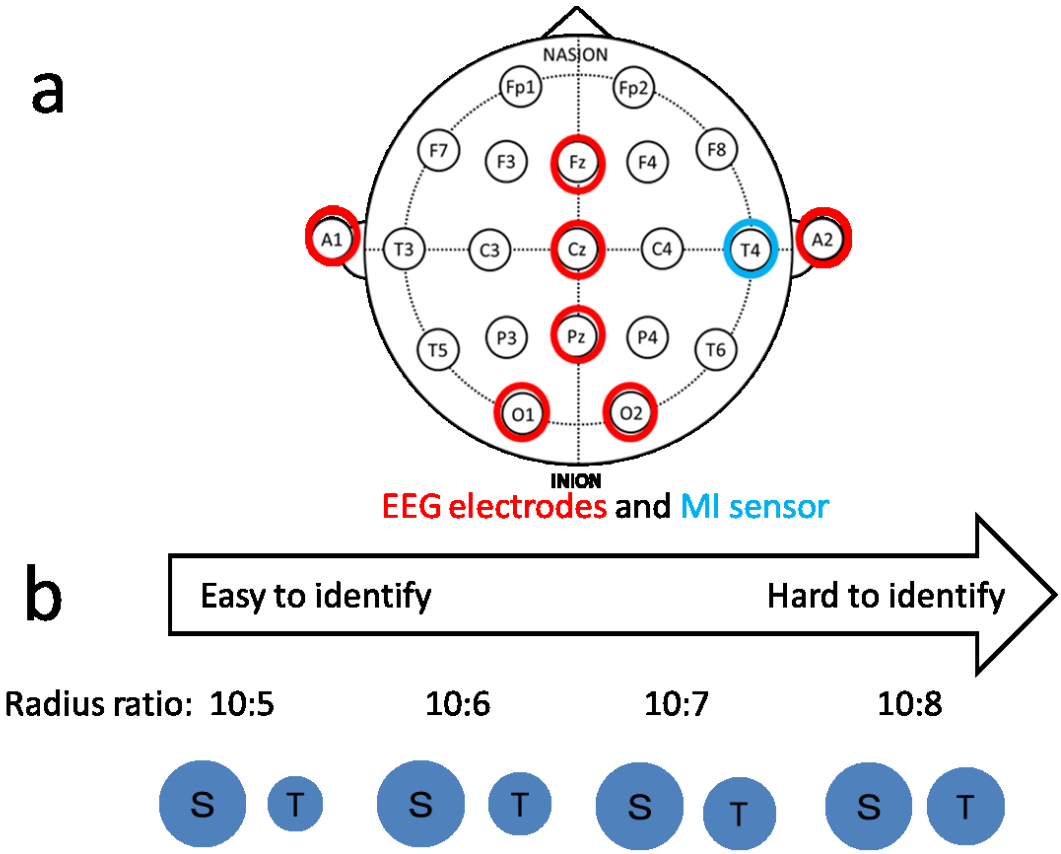

Figure 4.12 (a) Positions the EEG electrodes and MI sensor were set up. (b)4 pairs of visual stimuli with different radius ratio (S:T).

In this task, there are 280 visual stimuli (224 standard and 56 target), which has a 10:5 radius ratio, were frequently presented in a random series once every 840 ms (420ms duration and 420 ms interval time). And the experiment repeated 3 times in other three radius ratio. In order to compare the result with the EEG, I set our processing moduel as the same as the EEG's, which the passband of the BPF is from 1-5 Hz, and 30 standard and target conditions were chosen for arithmetic averaging.

The brain activity of both target and standard conditions were processed in the same fashion. As the standard conditions were usually as a reference in the comparing, I outputted the difference between targer and standard conditions. The results are shown in figure 4.13.

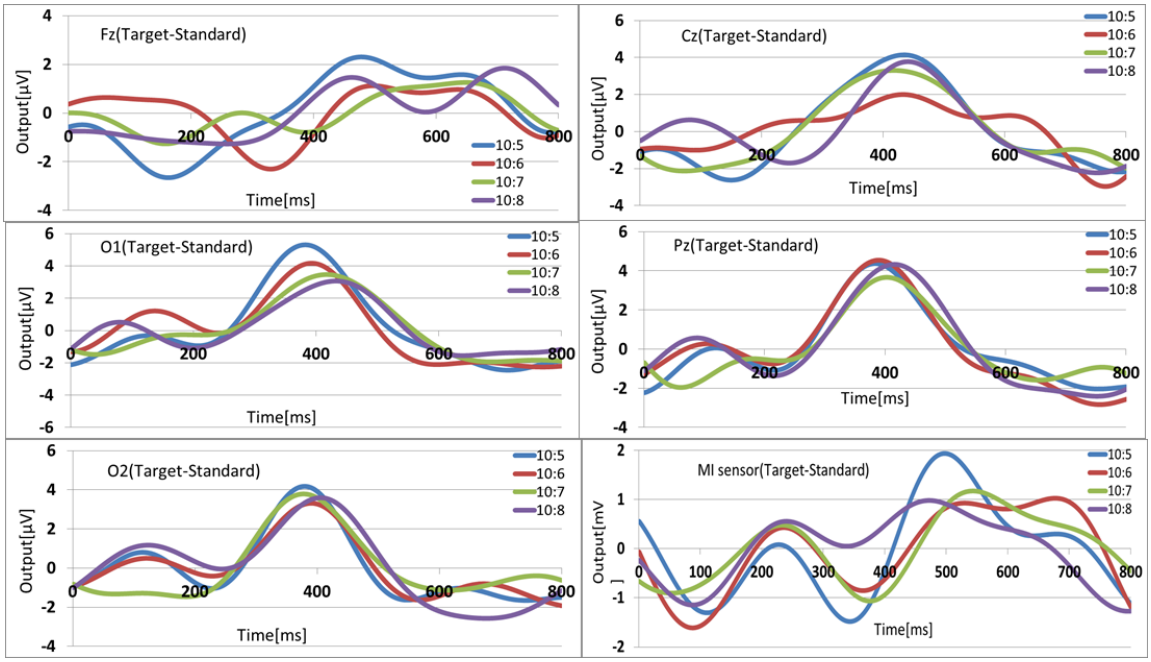

Figure 4.13 P300 ERP/ERF Waveforms in different standard/target radius ratio and positions. From left side: Fz, O1 and O2 positions measured by EEG. Right side: Cz, Pz positions measured by EEG and T4 position measured by MI sensor. The blue, red, green and purple lines represent different radius ratio of stimuli.

It is obviously that the latency of deflections in both EEG electrodes and MI sensor measurement is about 300-500 ms. However, most of the EEG deflections have a single positive peak but the deflections of MI sensor have two peaks, one is positive and the other is negetive.

Chapter 5

Measurement of Multi-channel Real-time/Off-line System

5.1 Principle of Independent Component Analysis

In this study, I expect to obtain a better S/N ratio of the brain activity, so the system was be improved to a multi-channel system to reduce the noise produced by the body using Independent Component Analysis, one of the multivariate statistics.

Independent Component Analysis (ICA) is a statistical and computational method to separate independent sources linearly mixed in several sensors. It is a special case of Blind Source Separation (BSS) and has many practical applications in digital signal processing area, including face recognition, mobile communications and removing artifacts from brain signals.

5.1.1 Basic theory of ICA

The ICA was created to resolve the so-called cocktail party problem as shown in figure 5.1. The problem is described as: Assuming three people are speaking simultaneously at a party which with all kinds of background noise

like music or voices from other people. Several microphones are placed at different locations around those three people to record their words. When we hear the records later, the voices of those three people would be difficult to identify respectively as they were mixed up. So the problem is defined to separate out the different voices of speakers (sources) from those mixed records (mixtures) with as little distortion as possible.

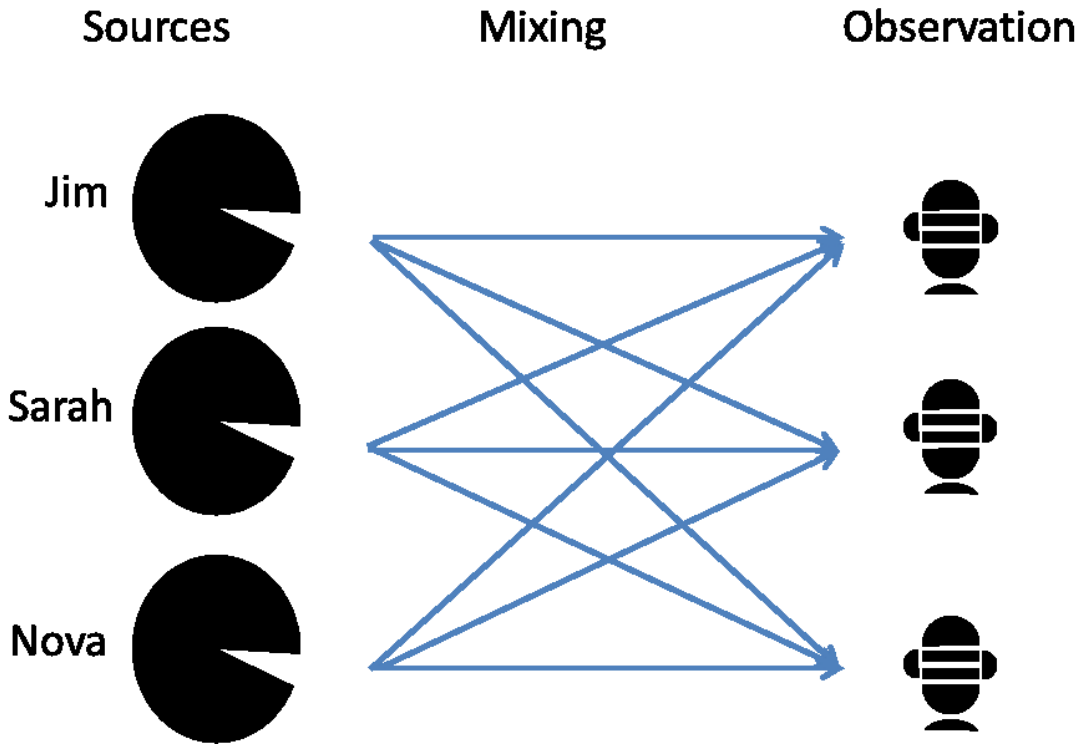

Figure 5.1 The schematic diagram of the cocktail part problem

We denote the mixed records as $x_1(t)$, $x_2(t)$ and $x_3(t)$. Each element of these records is a weighted sum of the signals originated from the three people, which we denote as $s_1(t)$, $s_2(t)$ and $s_3(t)$. So it is expressed as:

$$x_1(t) = a_{11}s_1(t) + a_{12}s_2(t) + a_{13}s_3(t) \quad (5.1)$$

$$x_2(t) = a_{21}s_1(t) + a_{22}s_2(t) + a_{23}s_3(t) \quad (5.2)$$

$$x_3(t) = a_{31}s_1(t) + a_{32}s_2(t) + a_{33}s_3(t) \quad (5.3)$$

Where a_{ij} are the weighted parameters that depend on the distances between microphones and the three people. In general situation, if the number of speakers is n and we use m microphones to record the signals. It would be expressed as:

$$x_1(t) = a_{11}s_1(t) + a_{12}s_2(t) + \cdots + a_{1n}s_n(t) \quad (5.4)$$

$$x_2(t) = a_{21}s_1(t) + a_{22}s_2(t) + \cdots + a_{2n}s_n(t) \quad (5.5)$$

$$\cdots \quad (5.6)$$

$$x_m(t) = a_{m1}s_1(t) + a_{m2}s_2(t) + \cdots + a_{mn}s_n(t) \quad (5.7)$$

It could also be simply denoted in matrix as:

$$\begin{pmatrix} x_1(t) \\ \vdots \\ x_m(t) \end{pmatrix} = \mathbf{A} \begin{pmatrix} s_1(t) \\ \vdots \\ s_n(t) \end{pmatrix} \quad (5.8)$$

$$\mathbf{x} = \mathbf{A}\mathbf{s} \quad (5.9)$$

Where A is the $m \times n$ matrix of weighted parameters, also called mixing matrix. As the number of microphones are usually fit the number of speakers, we assume n = m, thus $\mathbf{A}$ is a square matrix.

Then we can compute the inverse matrix of $\mathbf{A}$, $\mathbf{W} = \mathbf{A}^{-1}$, and the equation 5.9 becomes:

$$\mathbf{s} = \mathbf{W}\mathbf{x} \quad (5.10)$$

In this equation, the records matrix $\mathbf{x}$ is all we get, the unmixing matrix $\mathbf{W}$ and sources matrix (independent components, ICs) $\mathbf{s}$ are assumed to be unknown and the main goal of ICA is to find the $\mathbf{W}$ and $\mathbf{s}$ using $\mathbf{x}$.

There are also two ambiguities when use ICA:

1: The scaling and sign of the ICs can not be determined. For example, if the mixing matrix $\mathbf{A}$ times a constand α, $\mathbf{A}' = \alpha\mathbf{A}$, and the ICs $\mathbf{s}$ times $1/\alpha$, $\mathbf{s}' = \mathbf{s}/\alpha$,

$$\mathbf{x} = \mathbf{A}'\mathbf{s}' = \alpha\mathbf{A}\frac{\mathbf{s}}{\alpha} = \mathbf{A}\mathbf{s} \tag{5.11}$$

The records matrix $\mathbf{x}$ would be as same as the equation 5.9.

2: The order of the ICs can not be determined. Assuming n = m = 3,

$$\begin{pmatrix} x_1(t) \\ x_2(t) \\ x_3(t) \end{pmatrix} = \begin{pmatrix} a_{11} & a_{12} & a_{13} \\ a_{21} & a_{22} & a_{23} \\ a_{31} & a_{32} & a_{33} \end{pmatrix} \begin{pmatrix} s_1(t) \\ s_2(t) \\ s_3(t) \end{pmatrix} \tag{5.12}$$

If we change the order of $\mathbf{A}$ and $\mathbf{s}$,

$$\begin{pmatrix} x_1(t) \\ x_2(t) \\ x_3(t) \end{pmatrix} = \begin{pmatrix} a_{12} & a_{13} & a_{11} \\ a_{22} & a_{23} & a_{21} \\ a_{32} & a_{33} & a_{31} \end{pmatrix} \begin{pmatrix} s_2(t) \\ s_3(t) \\ s_1(t) \end{pmatrix} \tag{5.13}$$

The results would be as same as the equation 5.12.

The fundament of using ICA is that the sources $\mathbf{s}$ must be statistically independent and those ICs must be non-gaussian (non-normal distribution), as the multivariate standard normal distribution is rotationally symmetric and the mixing matrix A is not identifiable for gaussian ICs [43, Chapter 2, 7]. There are two methods that mostly used in ICA estimations, minimization of mutual information and maximization of non-gaussianity. In this study, I used the second method.

5.1.2 Measurement of non-gaussianity

The maximization of non-gaussianity depends on measurement of non-gaussianity. Two methods, as Kurtosis and Negentropy, are normally used in the measurement. First of all, a non-gaussian random variable y is defined. In order to simplify the calculation of ICA, we assume that the mean of y is zero (centering), $\mu_y = E[y] = 0$, and variance is one (whitening), $\sigma_y{}^2 = E\left[\left(y - \mu_y\right)^2\right] = 1$.

The (excess) kurtosis of y is defined as:

$$kurt(y) = E[y^4] - 3(E[y^2])^2 = E[y^4] - 3 \qquad (5.14)$$

It measures the spikiness of a distribution and when y is a non-gaussian random variable, as we assumed, the kurtosis is non-zero (positive if y is spikier than a guassian, or negative if y is flatter), and if y is a gaussian random variabvl, the kurtosis will be zero (the kurt(y) equals 3 for a gaussian y when using the kurtosis function of matlab R2013a student version). However, kurtosis is very sensitive to outliers which could reduce the robustness of the measurement [43, Chapter 8].

The other method of non-gaussianity measurement is given by negentropy, which based on the information theory and used to measure the distance to normality. From the information theory, the differential entropy of y, with a density function p(y), is defined as:

$$H(y) = -\int p(y)\log f(y)dy \qquad (5.15)$$

As the gaussian variable has the highest entropy among all distributions with the same mean and variance, the entropy difference between a gaussian

distribution, y_G, which have the same mean and variance as y, and y, is defined as the negentropy J(y):

$$J(y) = H(y_G) - H(y) \geq 0 \tag{5.15}$$

Unless y is a gaussian distribution, the J(y) will be always greater than zero. However, estimating the negentropy need to calculat the probability density function and it is difficult. So it is common to use approximations of negentropy, such as :

$$J(y) \propto \left[E[g(y)] - E[g(y_G)]\right]^2 \tag{5.16}$$

Where g are some functions that do not grow too fast, such as $g(y) = \tanh(ay)$, $1 \leq a \leq 2$ (often taken as a=1). It was proved very useful depend on [43, Chapter 8]. Since the $E[g(y_G)]$ is a constant so we will get the maximization of non-gaussianity J(y) by maximizing E[g(y)].

5.1.3 FastICA algorithm

FastICA was first invented by Aapo Hyvärinen at Helsinki University of Technology. It is a remarkable method that learning rule for finding a direction to get the maximum of the non-gaussianity based on a fixed-point iteration algorithm. Non-gaussianity is measured by $J(\mathbf{y}) = E[g(\mathbf{w}^T\mathbf{x})]$ given in equation 5.16. According to the Kuhn-Tucker conditions [43, Chapter 3], the optima of $E[g(\mathbf{w}^T\mathbf{x})]$ can be get at points:

$$E[\mathbf{x}g(\mathbf{w}^T\mathbf{x})] - \beta\mathbf{w} = 0 \tag{5.17}$$

Under the constraint that $E[(\mathbf{w}^T\mathbf{x})^2] = \|\mathbf{w}\|^2 = 1$. Then solve the equation 5.17 iteratively using Newton's method,

$$J_F(\mathbf{w}) = \frac{\partial F}{\partial \mathbf{w}} = E[\mathbf{x}\mathbf{x}^T g'(\mathbf{w}^T\mathbf{x})] - \beta\mathbf{I} \quad (5.18)$$

Where $J_F(\mathbf{w})$ is the Jacobian matrix of function $F(\mathbf{w})$, which denotes the left side of equation 5.17. Then since the $\mathbf{x}$ is whited, the $E[\mathbf{x}\mathbf{x}^T g'(\mathbf{w}^T\mathbf{x})]$ can be approximated as:

$$E[\mathbf{x}\mathbf{x}^T g'(\mathbf{w}^T\mathbf{x})] \approx E[\mathbf{x}\mathbf{x}^T]\, E[g'(\mathbf{w}^T\mathbf{x})] = E[g'(\mathbf{w}^T\mathbf{x})]\mathbf{I} \quad (5.19)$$

The Jacobian matrix becomes diagonal maxtrix:

$$J_F(\mathbf{w}) = [E[g'(\mathbf{w}^T\mathbf{x})] - \beta]\mathbf{I} \quad (5.20)$$

And the Newton iteration becomes:

$$\mathbf{w}_{+1} = \mathbf{w} - \frac{[E[\mathbf{x}g(\mathbf{w}^T\mathbf{x})] - \beta\mathbf{w}]}{E[g'(\mathbf{w}^T\mathbf{x})] - \beta} \quad (5.21)$$

Where $\mathbf{w}_{+1}$ is the updated weight matrix. Then multiplying both sides by the scaler $\beta - E[g'(\mathbf{w}^T\mathbf{x})]$, equation 5.21 will become:

$$\mathbf{w}_{+1} = E[\mathbf{x}g(\mathbf{w}^T\mathbf{x})] - E[g'(\mathbf{w}^T\mathbf{x})]\mathbf{w} \quad (5.22)$$

At last, the basic form of the FastICA algorithm used in this study is as:

1: Finding the size of the observed signal matrix $\mathbf{x}$, assuming the size is $m \times n$, which m is the number of sensors and n is the number of elements in each data series.

2: Centering the matrix $\mathbf{x}$ to make the mean in every row is zero.

3: Whitening the matrix $\mathbf{x}$ to make its components uncorrelated and their variances equal unity.

4: Create a random weight $m \times m$ matrix $\mathbf{w}$.

5: Setting a maximization count of the lteration, C_{max}.

6: Run the Iteration of equation 5.22

7: Normalize $w = \frac{w_{+1}}{\|w_{+1}\|}$, and if it is not converged, back to step 6. And if

C > C_{max}, stop the program as there might be no optima of **w**.

The flowchart is shown in figure 5.2

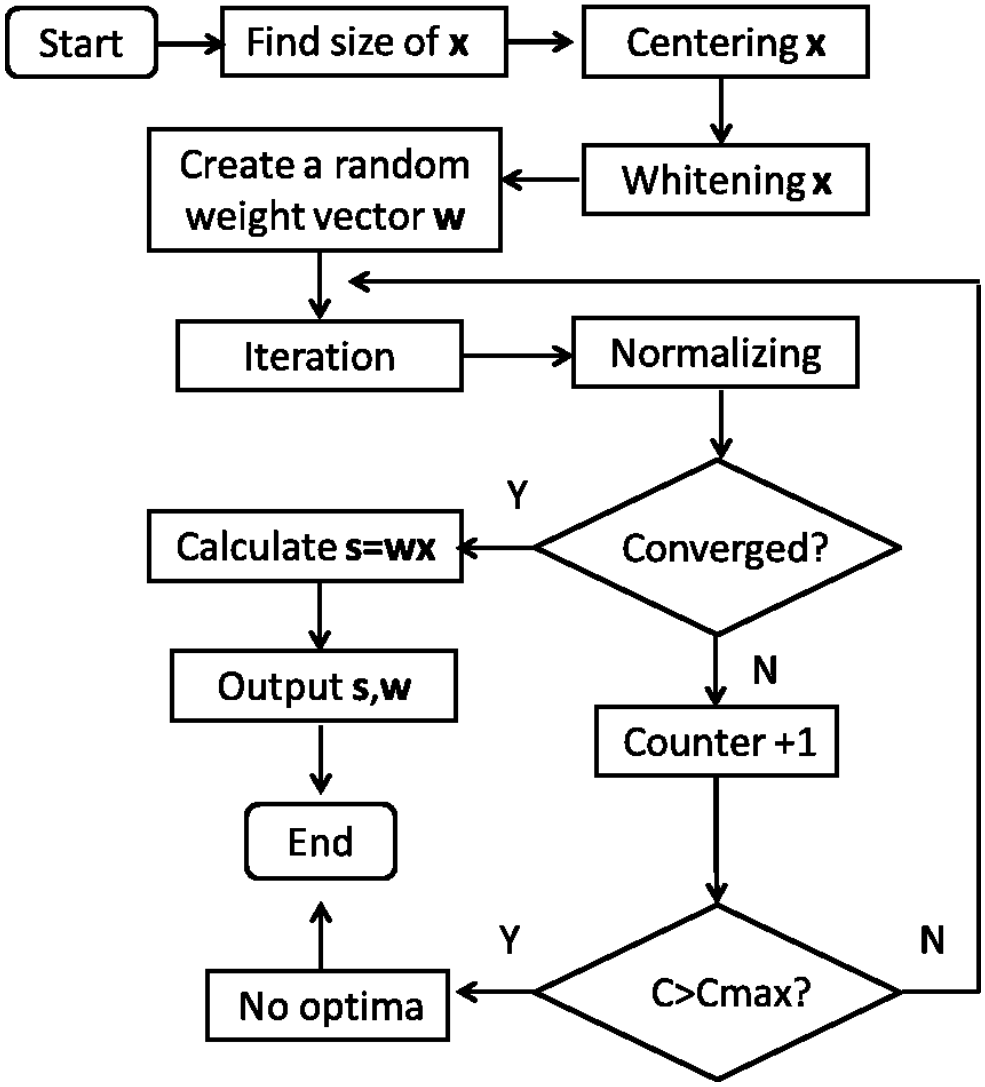

Figure 5.2 Flowchart of a FastICA algorithm

5.2 Measurement of P300 ERF (Multi-channel)

5.2.1 The Multi-channel system

In this study, I used three MI sensors to construct the multi-channel measurement system as shown in figure 5.3. The sensor heads were fixed into a Soft Polyfoam which can cover the subject head. The distances between those three sensor heads was set to 4 cm. The detection characteristics is shown in figure 5.4, and based on this results they are considered as the same sensitivity.

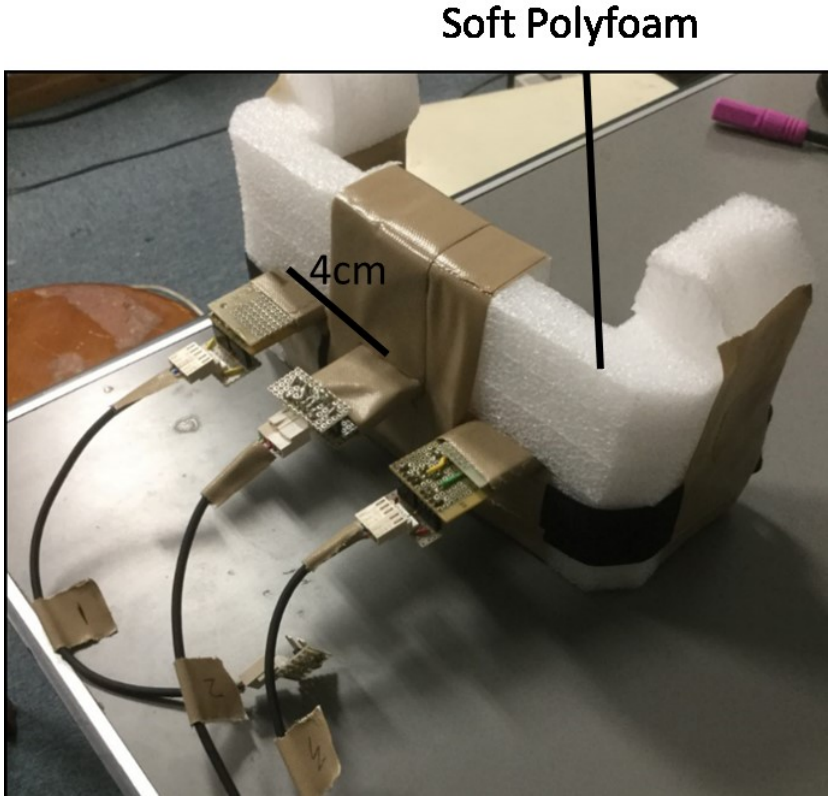

Figure 5.3: Multi-channel measurement system including three MI sensors

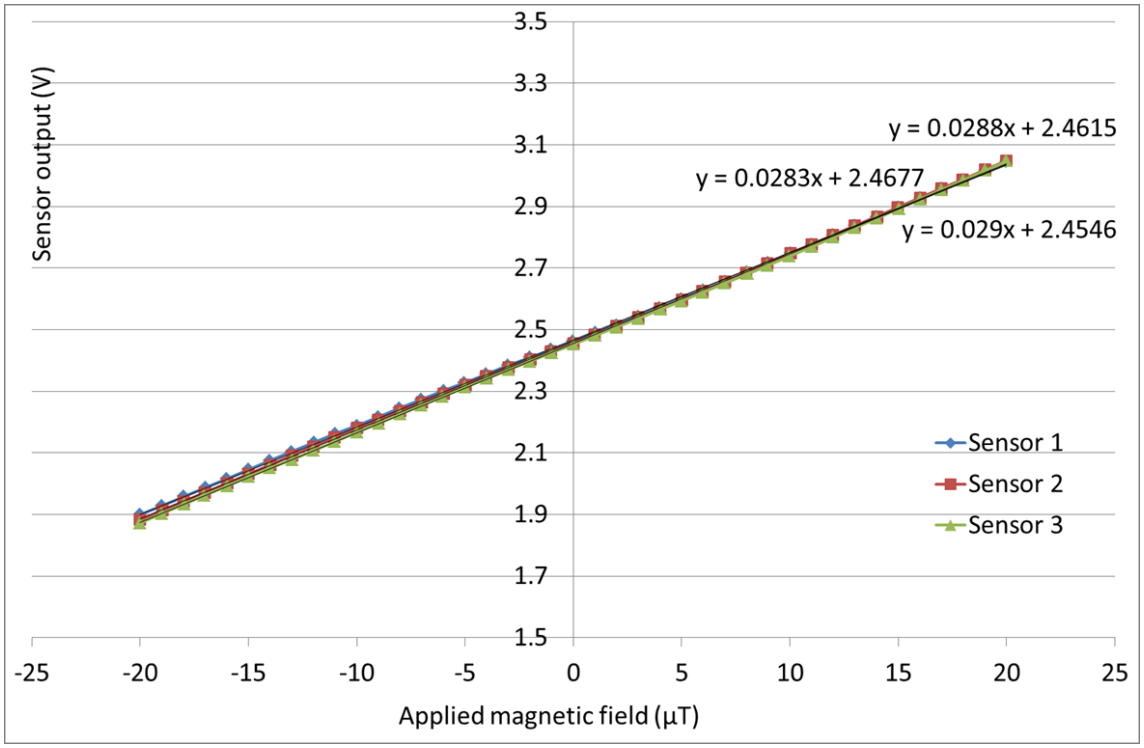

Figure 5.4 Detection characteristics of the three MI sensor used in the multi-channel system.

5.2.2 The P300 ERF measurement

On the measurement of P300 ERF using multi-channel system, the three sensors were set on the position around Pz, P3 and P4. As with the measurement using single-channel system, the passband of main digital filter was 1-9 Hz, the range filter was applied to remove the data with over range. Then the data were divided into the standard and target conditions. The difference is that the divided data were saved and outputted to do a off-line FastICA. After separating the independent sources, the ICs look like artifacts (depending on their features in time and frequency domain) and

their weighted parameters will be manually removed. Then the rest of the ICs will be remixed to recover the divided data. At last, 50 standard and target conditions were chosen from those divided data for arithmetic averaging in the same method respectively. The different between those two processing is shows in figure 5.5.

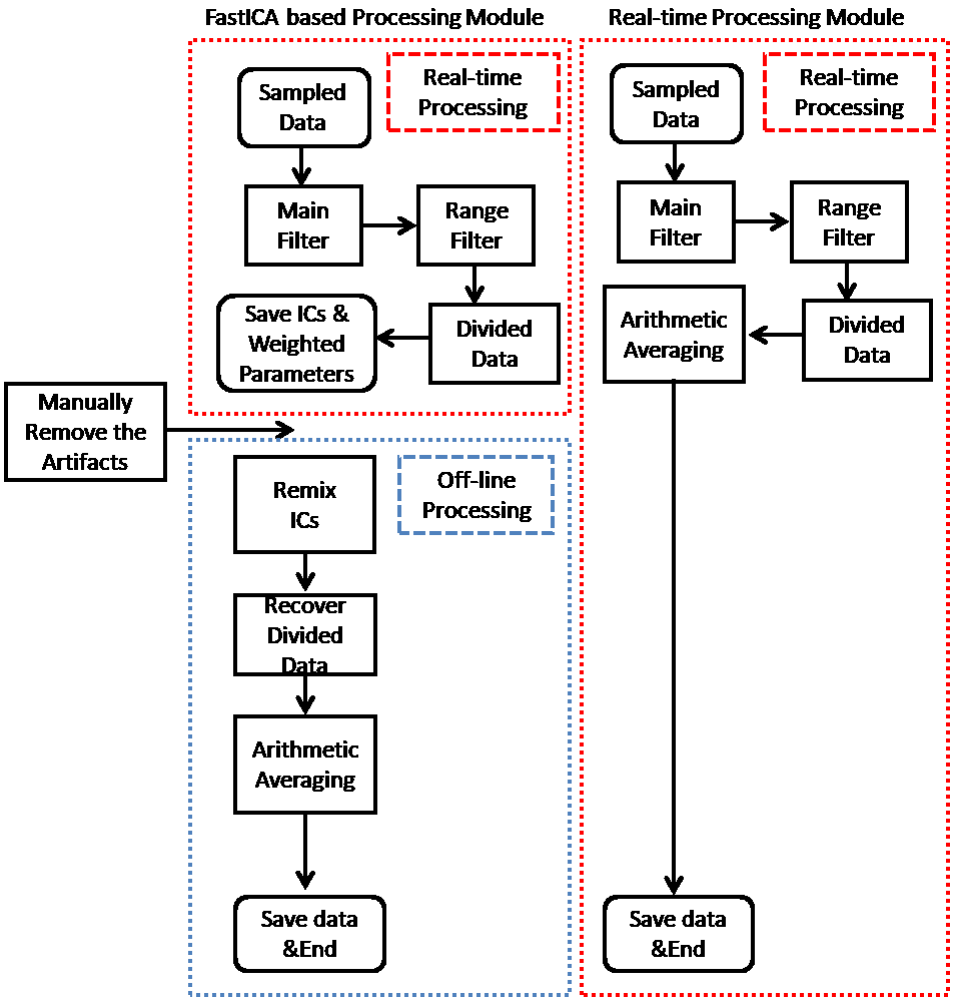

Figure 5.5 The different between real-time processing module and the FastICA based processing module.

The waveforms of P300 ERF obtained were comparing with normal processing which as with the real-time P300 ERF processing, as shown in figure 5.6.

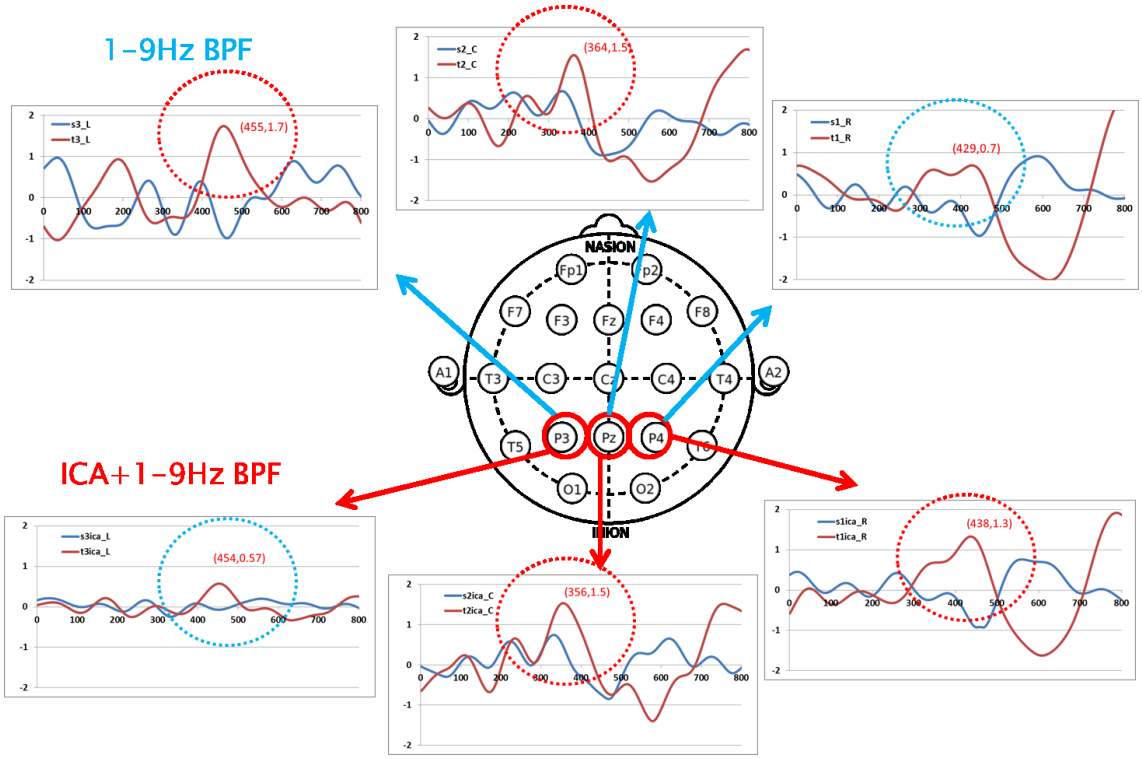

Figure 5.6 The averaged P300 brain activity waveforms measured around the position of Pz, P3 and P4 using a multi-channel MI system. The three waveforms on top are based on the real-time p300 processing module discussed in Chapter 4, and the waveforms on the bottom are used the digital filter and FastICA.

From the results, it is obviously that all the waveforms on Pz and P4 show similar characteristics, but on P3, the peak of waveform processed by FastICA based processing module (left-bottom) is weaker than that of waveform processed by the real-time processing module.

5.2.3 Discussion

In order to confirm the performance of the FastICA module, I have run a test program to confirm the performance of FastICA module.

Step one: Four signals were created as sources, each of them has a frequency band of 7-13 Hz, 1-9 Hz, 0.1-2 Hz and the last one is a white noise as shown in figure 5.7. They are unknown in real measurement, thus the FastICA module is designed to estimate them based on the observed data mixed signals).

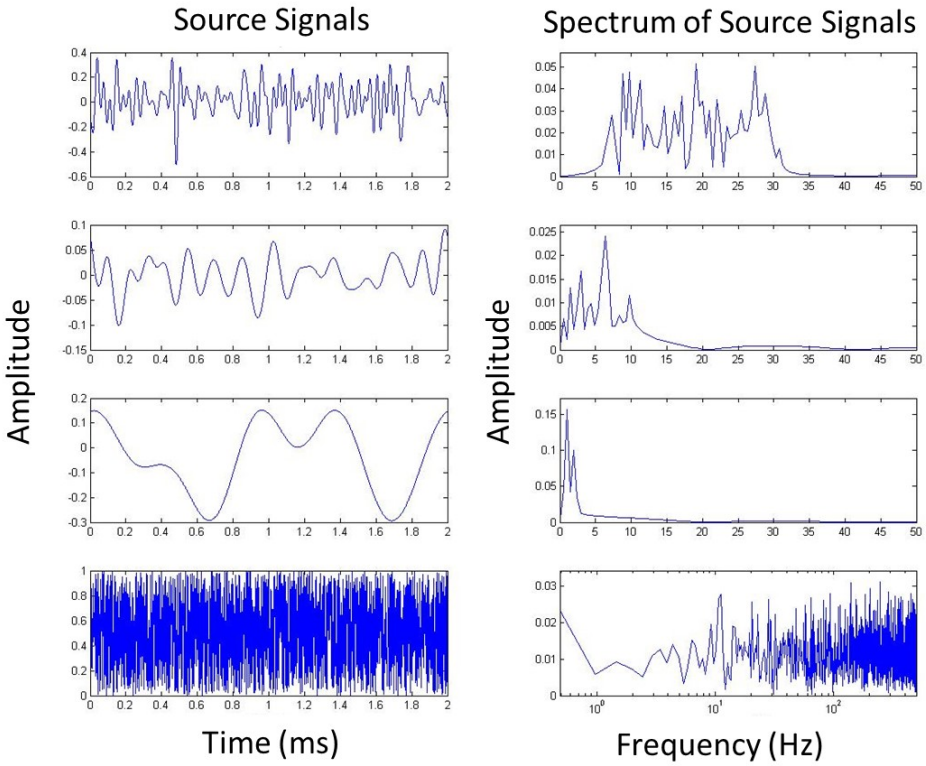

Figure 5.7 Created source signals with frequency band of 7-13 Hz, 1-9 Hz, 0.1-2 Hz and the last one is a white noise.

Step two: Mixed those four source signals using a random matrix (also unknown in real measurement), then the observed data are obtained. They are known in real measurement as the data recorded by sensors, as shown in figure 5.8.

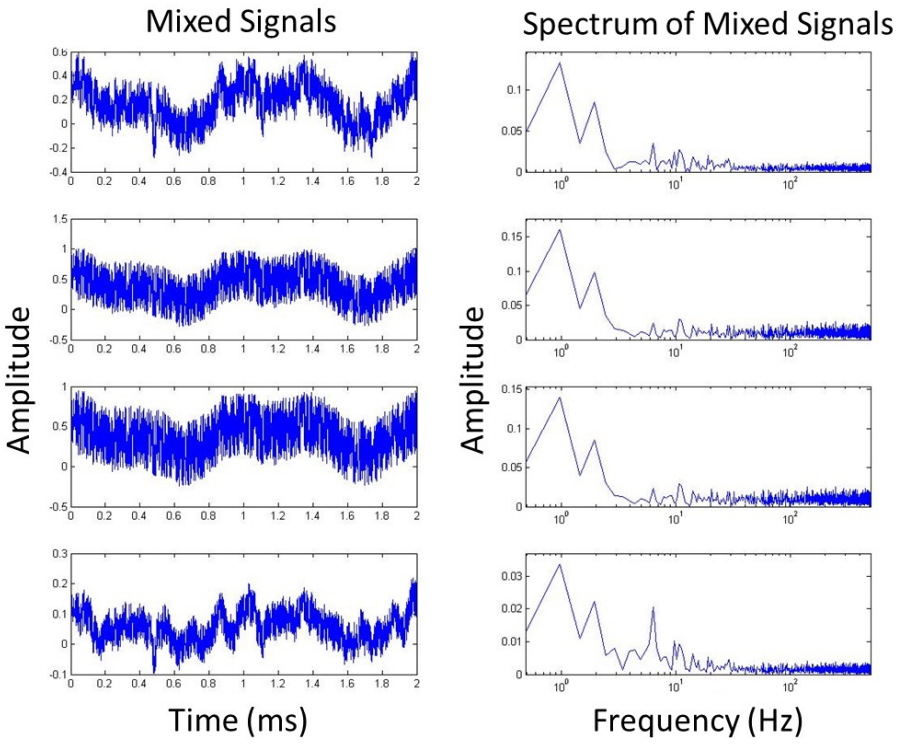

Figure 5.8 The four source signals are mixed by a random matrix, the observed data

Step three: Run the FastICA module to separate the the observed data into ICs and compare those ICs with the source signals to confirm the performance. The separated ICs are show in figure 5.9. It is obviously that the separated ICs have extremely similar characteristics with those source signals shown in figure 5.7. And the performance of the FastICA module is confirmed. In this study, the waveforms like 2 and 3 were considered as

noise(white and body movement noise). They will be removed.

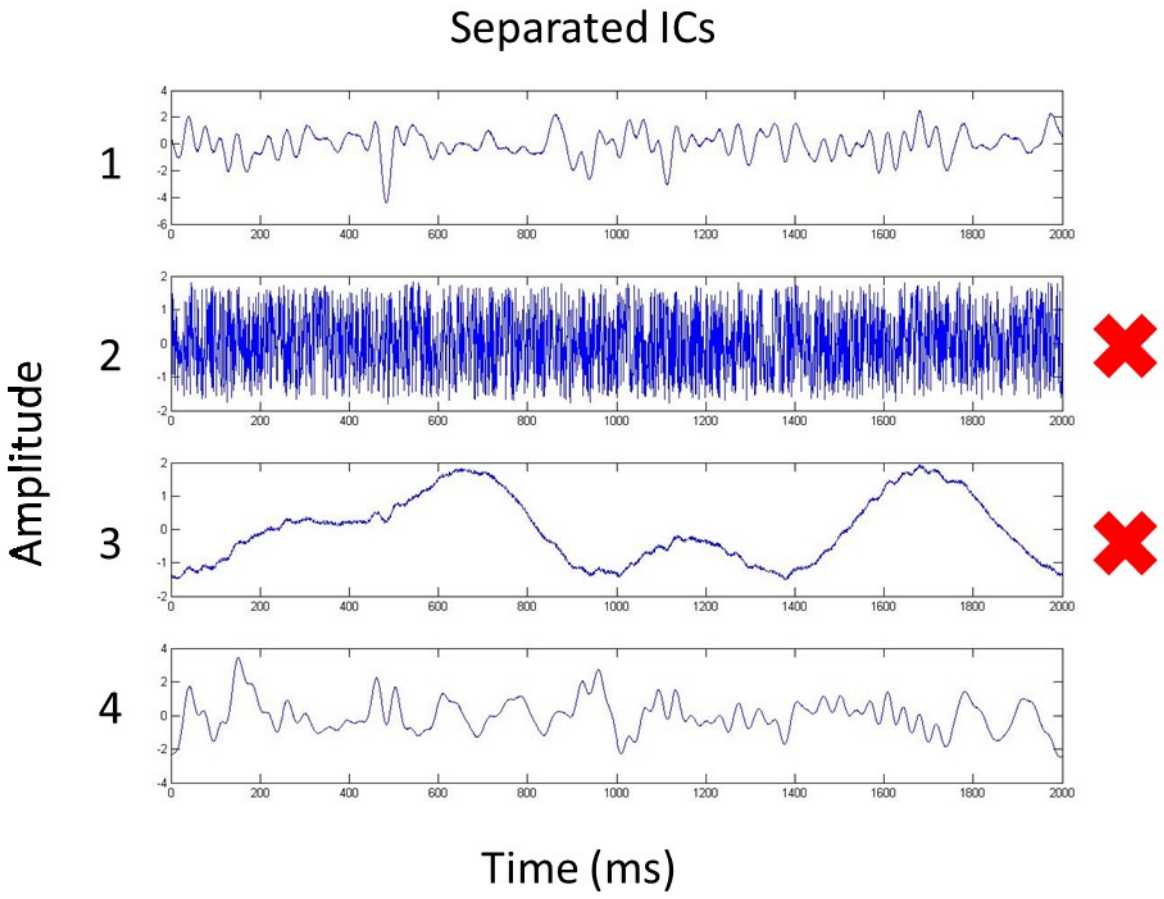

Figure 5.9 The ICs separated from observed data. It is obviously that the separated ICs have extremely similar characteristics with those source signals shown in figure 5.7. In this study, the waveforms like 2 and 3 were considered as noise(white and body movement noise). They will be removed.

Chapter 6

Conclusions & Future work

6.1 Conclusions

The main goal of this study was to develop and improve the brain activity measurement system based on the MI sensor. In this study, I constructed and updated the multi-function brain activity measurement system based on highly sensitive MI sensor. I measured the N100 AEF in left and right temporal regions, the P300 ERF induced by auditory stimuli in parietal region, alpha rhythm in occiptial region and the P300ERF induced by visual stimuli in frontal, parietal, left and right temporal regions using both real-time and off-line processing module. After comparing our results with other relevant research, the reliability of the system was confirmed and it presents the capabilities of the MI brain activity measurement system, as a small-scale, low-cost and highly sensitive magnetic sensor, for applications of biomagnetic field measurement.

6.2 Future work

In the next step, first I expect to improve the FastICA based signal processing module, it has been proved that the FastICA is a powerful tool to separate the mixed signals for reducing the noise that can not be easily removed by frequency filter. But it will be hard to use and easy to make mistakes if all the artifacts have to be chosen by a operator. It needs to be improved and tested with more experiments and more subjects. On the other hand, I am thinking about making the circuit all into digital using a field-programmable gate array (FPGA) to obtain a lower noise level and a more integrated multi-channel system. At last, I think the S/N ratio of the system need to be improved to obtain more accurate data for measuring brain activity.

Reference

[1] http://www.neuracles.com/sciences/sciences.asp

[2] Michael Jeffrey Aminoff, “Electrodiagnosis in Clinical Neurology”, Elsevier Health Sciences, Jan 1, 2012, Chapter 3.

[3] Jan van Erp, Fabien Lotte and Michael Tangermann, “Brain-computer interfaces: beyond medical applications”. Computer, Volume: 45, Issue: 4, April 2012, p26–34.

[4] Leigh R Hochberg et al, “Reach and grasp by people with tetraplegia using a neurally controlled robotic arm”, May 2012Nature 485(7398):372-5

[5] Nishant Mehta, Sadhir Hussain and Melody Moore Jackson, “Optimal Control Strategies for an SSVEP-Based Brain-Computer Interface”, January 2011 International Journal of Human-Computer Interaction 27 (1): 85-101

[6] Karl Lafleur et al, “Quadcopter control in three-dimensional space using a noninvasive motor imagery-based brain–computer interface”, 2013 J. Neural Eng. 10 046003

[7] Cathrine. Christiansen, “X-ray contrast media—an overview”, Toxicology. 209 (2005): pp186

[8] Donald W. McRobbie, Elizabeth A. Moore, Martin J. Graves and Martin R. Prince, “MRI From Picture to Proton”, Cambridge University Press, Chapter 3.

[9] 生体磁気計測 / 小谷誠 [ほか] 共著. -- コロナ社, 1995.10. -- (医用工学シリーズ 9). Chapter 1.

[10] T. Miyazaki and N. Tezuka, J. Magn. Magn. Mater. 139, L231 (1995).

[11] K. M. H. Lenssen, D.J. Adelerhof, H.J. Gassen, A.E.T. Kuiper, G.H.J. Somers, and J.B.A.D. van Zon, Sens. Actuators A 85, 1 (2000).

[12] S. C. Mukhopadhyay, K. Chomsuwan, C. P. Gooneratne and S. Yamada, IEEE Sens. J. 7, 401 (2007).

[13] Candid Reig, et al, "Magnetic Field Sensors Based on Giant Magnetoresistance (GMR) Technology: Applications in Electrical Current Sensing", Sensors 2009, 9, 7919-7942; doi:10.3390/s91007919

[14] Pavel Ripka, "Advances in fluxgate sensors", Volume 106, Issues 1–3, 15 September 2003, p8-14

[15] https://www.dreamstime.com/royalty-free-stock-photo-normal-brain-waves-eeg-image29444815

[16] G. P. Jacobson, "Magnetoencephalographic studies of auditory system function," J. Clin. Neurophysiol. 11(3), 343–364 (1994).

[17] K. Wang, S. Tajima , Y. Asano , Y.Okuda , N. Hamada , C. Cai , and T. Uchiyama, "Detection of P300 brain waves using a MagnetoImpedance sensor", Proceedings of the 8th International Conference on Sensing Technology, pp547-550

[18] K. Wang, S. Tajima, D. Song, N. Hamada, C. Cai, and T. Uchiyama, "Auditory evoked field measurement using magneto-impedance sensors", Journal of Applied Physics 117, 17B306 (2015)

[19] Kewang Wang, Changmei Cai, Michiharu Yamamoto, and Tsuyoshi Uchiyama, "Real-time brain activity measurement and signal processing system using highly sensitive MI sensor", AIP Advances 7, 056635 (2017)

[20] K. Mohri, T. Kohhzawa, K. Kawashima, H. Yoshida and L.V. Panina, IEEE Trans. Magn. 28, 3150 (1992).

[21] K. Mohri, Mat. Sci. Eng. A—Structural Mat. Prop. Microstructure Proc. 185, 141 (1994), (Paper is presented at the RQ-8 Conf., Sendai, Aug. 1993)

[22] L. V. Panina and K. Mohri, "Magneto-Impedance Effect in Amorphous Wires", Appl. Phys. Lett. 65, 1189-1191 (1994).

[23] L. V. Panina, K. Mohri, K. Bushida and M. Noda, J. Appl, Phys. 76, 6198 (1994)

[24] T. Kanno, K. Mohri, T. Yagi, T. Uchiyama and L. P. Shen, "Amorphous Wire MI Micro Sensor Using C-MOS IC Multi-vibrator", IEEE Trans. Magn., Vol.33, No.5, pp.3353-3355.

[25] T. Uchiyama, N. Hamada and C. Cai, "Development of Multicore Magneto-Impedance Sensor for Stable Pico-Tesla Resolution", 7th International Conference on Sensing Technology (ICST 2013), p573-577. DOI: 10.1109/ ICSensT.2013.6727718

[26] Tsuyoshi Uchiyama, Norihiko Hamada, and Changmei Cai, "Highly Sensitive CMOS Magnetoimpedance Sensor Using Miniature Multi-Core Head Based on Amorphous Wire", IEEE TRANSACTIONS ON MAGNETICS, VOL. 50, NO. 11, NOVEMBER 2014.

[27] J. Virtanen, J. Ahveninen, R. J. Ilmoniemi, R. Naatanen, and E. Pekkonen, "Replicability of MEG and EEG measures of the auditory N1/N1mresponse," Electroencephalogr. Clin. Neurophysiol. 108(3), 291–298 (1998)

[28] R. Naatanen and T. Picton, “The N1 wave of the human electric and magnetic response to sound: A review and an analysis of the component structure,” Psychophysiology 24(4), 375–425 (1987).

[29] Steven A Hillyard, Robert F Hink, Vincent L Schwent, Terence W Picton, “Electrical signs of selective attention in the human brain”. Science. 182 (4108): 177–180. (1973)

[30] J. Polich and C. Margala, “P300 and probability: Comparison of oddball and single-stimulus paradigms,” Int. J. Psychophysiol. 25, 169–176 (1997).

[31] Jose L. Cantero, Mercedes Atienza, Rosa M. Salas, “Human alpha oscillations in wakefulness, drowsiness period, and REM sleep: different electroencephalographic phenomena within the alpha band,” Neurophysiol Clin 2002 ; 32 : 54-71.

[32] G. Pfurtscheller, A. Aranibar, “Event-related cortical synchronization detected by power measurements of scalp EEG”, Electroencephalography and Clinical Neurophysiology , 1977, 42:817—826.

[33] Wolfgang Klimesch, Paul Sauseng, Simon Hanslmayr, “EEG alpha oscillations: The inhibition–timing hypothesis”, BRAIN RESEARCH REVIEWS 53 (2007), p63-88.

[34] G. Pfurtschellera, F. H. Lopes da Silva, “Event-related EEG/MEG synchronization and desynchronization: basic principles”, Clinical Neurophysiology 110 (1999), p1842-1857.

[35] Niedermeyer E, da Silva FL (2004) Electroencephalography: basic principles, clinical applications, and related fields.

[36] Keiichi MIMURA, “ON THE PERIODIC FLUCTUATIONS OF ALPHA WAVES”, Jap. J. Physiol., 21, 375-386, 1971.

[37] Kei Omata, Takashi Hanakawa, Masako Morimoto, and Manabu Honda, “Spontaneous Slow Fluctuation of EEG Alpha Rhythm Reflects Activity in Deep-Brain Structures: A Simultaneous EEG-fMRI Study”, PLoS One. 2013; 8(6): e66869, Issue 6, Volume 8.

[38] Ciulla. C, Takeda. T, Endo. H. “MEG characterization of spontaneous alpha rhythm in the human brain, ” Brain Topography, Volume 11, Number 3,1999.

[39] T. H. Sander, J. Preusser, R. Mhaskar, J. Kitching, L. Trahms, and S. Knappe, “Magnetoencephalography with a chip-scale atomic magnetometer”, Biomed Opt Express. 2012 May 1; 3(5): 981–990.

[40] Mecklinger, B. Maess, B. Opitz, E. Pfeifer, D. Cheyne, and H. Weinberg, “A MEG analysis of the P300 in visual discrimination tasks,” Electroencephalogr. Clin. Neurophysiol. 108, 45–56 (1998).

[41] Matti Hämäläinen, Riitta Hari, Risto J. Ilmoniemi, Jukka Knuutila, and Olli V. Lounasmaa, “Magnetoencephalography theory instrumentation and applications to noninvasive studies of the working human brain,” Rev. Mod. Phys. 65, 413 – Published 1 April 1993

[42] T. maeno, A. kaneko, K. Iramina, F. Eto, and S. Ueno, “Source modeling of the P300 event-related response using magnetoencephalography and electroencephalography measurements,” IEEE TRANSACTIONS ON MAGNETICS, VOL. 39, NO. 5, SEPTEMBER 2003.

[43] Aapo Hyvärinen, Juha Karhunen, and Erkki Oja, “Independent Component Analysis”, A Wiley-Interscience Publication JOHN WILEY & SONS, INC.

[44] A. C. Papanicolaou, R. L. Rogers, S. Baumann, C. Saydjari, and H. M. Eisenberg, “Source localization of two evoked magnetic field components using two alternative procedures,” Exp. Brain Res. 80, 44–48 (1990).

[45] H. H. Jasper: “The ten-twenty electrode system of the international federation,” Electroencephalography and clinical neurophysiology, Vol. 10, No. 2, pp. 371-375, 1958.

[46] 加賀 佳美, 相原　正男, “P300 基礎”, 臨床神経生理学 41 巻 2 号.

[47] John Stirling and Rebecca Elliott, “IntroducingNeuropsychology”, Psychology Press, 2002, Chapter 9.

[48] Miao-Kun Sun, “Cognitive Sciences at the Leading Edge”, Nova Publishers, 2008, Chapter 7.

[49] Timothy P. L. Roberts et al, “Latency of the Auditory Evoked Neuromagnetic Field Components: Stimulus Dependence and Insights Toward Perception”, Journal of Clinical Neurophysiology, 17(2): 114-129.

[50] S. Tajima, T. Uchiyama, Y. Okuda, and K. Wang, “Brain activity measurement in the occipital region of the head using a magnetoimpedance sensor,” 2013 Seventh International Conference on Sensing Technology (ICST), 267-270.

[51] J.Y. Bennington, and J.Polich, “Comparison of P300 from passive and active tasks for auditory and visual stimuli,” International Journal of Psychophysiology 34 (1999) 171-177.

[52] Klaus Linkenkaer-Hansen, Vadim V. Nikouline, J. Matias Palva and Risto J. Ilmoniemi, “Long-Range Temporal Correlations and Scaling Behavior in HumanBrain Oscillations”, The Journal of Neuroscience, February 15, 2001,21(4):1370–1377.

Acknowledgements

First of all, I would like to express my deep and sincere gratitude to my honorific supervisor, Graduate School of Engineering, Nagoya University, Associate Professor, Dr. Tsuyoshi Uchiyama, for giving me the great opportunity to be a part of the MI sensor research, for his continuous support of my Ph.D study, for his patience, understanding and immense knowledge. His guidance helped me all the time. During these years study in his laboratory, I not only learned the knowledge and skill, but also got a big family. I could not image to having a better advisor and mentor for my Ph.D study.

Beside my supervisor, I would like to extend my sincere appreciation to Prof. Takeshi Furuhashi, Prof. Satoshi Iwata and Prof. Minoru Hoshiyama for their valuable suggestions and encouragement. My gratitude also goes to ex-technical support officer, Oregon State University, Mr. Shingo. Tajima, thanks for his help and support when I was new here. I would like to express the appreciation to all my colleagues, Mr. Takashi Takiya, Mr. Ke Shi, Mr. Kohei Asano, Mr. Jiaju Ma, Ms. Hao Wang, Mr. Akihoro Higuchi, Mr. Takumi Tsuruha, Mr. Xindi Zhang and Mr. Ziqin Yang. I could not finish my experiments without your help.

My sincere thanks go to the Japan Student Services Organization (JASSO), which provided me with financial support during my Ph.D. and masters study, the Hattori Foundation, which provided me the dormitory, without their support and financial help, it would not have been possible for me to pursue and to complete this Ph.D. project successfully.

The most special thanks goes to my parents, thanks for their support, love, believing and understanding through all my life.

List of Publication

Papers		
Title	Journal	Authors
Auditory evoked field measurement using magneto-impedance sensors	Journal of Applied Physics 117, 17B306 (2015)	K. Wang, S. Tajima, D. Song, N. Hamada, C. Cai, and T. Uchiyama
Real-time brain activity measurement and signal processing system using highly sensitive MI sensor	AIP Advances 7, 056635 (2017)	Kewang Wang, Changmei Cai, Michiharu Yamamoto, and Tsuyoshi Uchiyama
Title	Proceedings paper	Authors
Detection of P300 brain waves using a MagnetoImpedance sensor	Proceedings of the 8th International Conference on Sensing Technology, pp547-550	K. Wang, S. Tajima , Y. Asano , Y.Okuda , N. Hamada , C. Cai , and T. Uchiyama
Brain activity measurement in the occipital region of the head using a magneto-impedance sensor	Proceedings of the 7th International Conference on Sensing Technology, pp267-270	S. Tajima, T. Uchiyama, Y. Okuda, and K. Wang

International Conferences		
Title	Conference	Authors
Detection of P300 brain waves in the parietal region using a Magneto-Impedance sensor	50th IEEE International Magnetics Conderence (InterMag 2014), Dresden, Germany, May 4-8, 2014.	K. Wang, S. Tajima , Y. Asano , Y.Okuda , N. Hamada , C. Cai , and T. Uchiyama

Domestic Conferences		
Title	Conference	Authors
高感度磁気インピーダンスセンサによる脳波 N100 および P300 信号の検出	第 38 回 日本磁気学会(慶応義塾大学) 2014 年9月 2～5日	王可望, 田島真吾, 内山剛, 中山晋介
一次グラジオメータ型 MI センサによる食品内異物検知	第 39 回 日本磁気学会(名古屋大学) 2015 年 9 月 8～11 日	滝谷 貴史, 王 可望, 内山 剛, 青山 均
高感度 MI センサによる誘発性脳磁場 N100 信号検出の試み	第 40 回日本磁気学会学術講演会(金沢大学) 2016 年 9 月 5～8 日	沈 清如, 王 可望, 内山 剛
高感度 MI センサを用いた視覚誘発 P300 脳磁場の計測と解析	平成 29 年電気学会全国大会(富山大学) 2017 年 3 月 15～17 日	浅野 光平, 内山 剛, 王 可望, 西田 貴樹